J. Mech. Phys. Solids 190 (2024) 105704

Contents lists available at ScienceDirect

Journal of the Mechanics and Physics of Solids

journal homepage: www.elsevier.com/locate/jmps

Quantized plastic deformation

N. Perchikov *, L. Truskinovsky

Laboratoire de Physique et Mécanique des Milieux Hétérogènes (PMMH), UMR7636 CNRS, ESPCI Paris, Université PSL, Université Paris Cité, Sorbonne Université, 7 Quai Saint-Bernard, 75005 Paris, France

ARTICLE INFO

Keywords:
Dislocations
Automaton
Crystal plasticity
Avalanches
Power-laws
Criticality

ABSTRACT

In engineering crystal plasticity inelastic mechanisms correspond to tensorial zero-energy valleys in the space of macroscopic strains. The flat nature of such valleys is in contradiction with the fact that plastic slips, mimicking lattice-invariant shears, are inherently discrete. A reconciliation has recently been achieved in the mesoscopic tensorial model (MTM) of crystal plasticity, which introduces periodically modulated energy valleys while also capturing in a geometrically exact way the crystallographically-specific aspects of plastic slips. In this paper, we extend the MTM framework, which in its original form had the appearance of a discretized nonlinear elasticity theory, by explicitly introducing the concept of plastic deformation. The ensuing model contains a novel matrix-valued spin variable, representing the quantized plastic distortion, whose rate-independent evolution can be described by a discrete (quasi-)automaton. The proposed reformulation of the MTM leads to a considerable computational speedup associated with the use of a robust and efficient hybrid Gauss-Newton–Cauchy energy minimization algorithm. To illustrate the effectiveness of the new approach, we present a detailed case-study focusing on the aspects of crystal plasticity that are beyond reach for the classical continuum theory. Thus, we provide compelling evidence that the re-formulated MTM is fully adequate to deal with the intermittency of plastic response under quasi-static loading. In particular, our numerical experiments show that the statistics of dislocational avalanches, associated with plastic yield in 2D square crystals, exhibits a power-law tail with a critical exponent matching the value predicted by general theoretical considerations and also independently observed in discrete-dislocation-dynamics (DDD) simulations.

1. Introduction

Recent experiments provided evidence that, at least in some types of crystals, quasi-static plastic flows involve intermittent, power-law distributed dislocation avalanches which generate scale-free dislocational patterns (Weiss et al., 2021). The associated plastic deformation cannot be simply homogenized, as it is not a sequence of uncorrelated events of similar size and is instead a highly correlated process spanning a broad range of spatial and temporal scales (Weiss et al., 2015). To rationalize this complex behavior, one has to go beyond the conventional continuum models and account adequately for the inherently discrete nature of plastic flows. The latter is neglected in the macroscopic engineering crystal plasticity (CP), where inelastic deformations are modeled by smooth elastically neutral mechanisms, operating in the space of macroscopic strains.

An alternative, strongly discrete perspective on crystal plasticity emerges from the microscopic standpoint where plastic deformation is viewed as a collection of interdependent lattice-invariant shears. Such shears represent cooperative displacements of atoms on crystallographically specific lattice planes and have a distinctly *quantized* nature.

* Corresponding author.
E-mail address: perchico@gmail.com (N. Perchikov).

https://doi.org/10.1016/j.jmps.2024.105704
Received 6 November 2023; Received in revised form 21 May 2024; Accepted 24 May 2024
Available online 27 May 2024

Several modeling tools have been developed to provide a lattice-scale description of crystal plasticity, ranging from microscopic molecular dynamics (Zepeda-Ruiz et al., 2017) and crystal phase-field approaches (Elder and Grant, 2004) to mesoscopic phase-field dislocation dynamics (Koslowski et al., 2002), discrete dislocation dynamics (Devincre et al., 2001), and continuum dislocation dynamics (Hochrainer et al., 2014). An attempt to bridge the entire range of scales from microscopic to macroscopic, while fully accounting for each of them, was made within the quasi-continuum framework (Miller and Tadmor, 2002). A highly peculiar nature of plastic flows in sub-micron crystals was addressed within the QCP (quantized crystal plasticity) theory, which is a CP-type approach adopting, phenomenologically, a discrete/quantized constitutive flow-rule calibrated based on data on single-dislocation slip events in nano-scale grains (Li et al., 2009, 2012). However, despite many successes in resolving specific sub-continuum features of crystal plasticity, see, for instance, Krebs et al. (2017), the ability of the existing approaches to capture the correct statistics of plastic fluctuations, while also accounting for large lattice rotations and adequately representing the crystallographic nature of lattice-invariant shears, remains rather limited.

An efficient conceptual interpolation between the microscopic, dislocation-based, and the macroscopic, continuum mechanics-based, models, has been recently proposed in the form of the mesoscopic tensorial model (MTM) of crystal plasticity (Salman and Truskinovsky, 2011, 2012; Zhang et al., 2020a; Baggio et al., 2019, 2023a; Salman et al., 2021; Baggio et al., 2023b). It operates with the macroscopic notions of stress and strain while capturing, in a geometrically exact way, the slip-generating mappings of crystal lattices onto themselves.

Interestingly, while the microscopic models are based on a system of ODEs and the macroscopic models are formulated in terms of a system of PDEs, the approach of MTM is intermediate, as it operates with mesoscopic discrete elements (DEs). The latter deform according to elastic constitutive relations while interacting through conventional mechanical forces, as in models of granular and particulate materials, see Cundall and Strack (1979), Wang et al. (2022), Rorato et al. (2021), Guo and Curtis (2015). The idea is that deformation below a certain mesoscopic length scale can be coarse-grained, with the resulting model still capturing correctly the intermittency and fractality above the cut-off.

The MTM approach can be viewed as a far reaching generalization of the 'purely elastic' toy models of crystal plasticity (Peierls, 1940; Nabarro, 1947; Frenkel, 1939; Prandtl, 1928). Using the depinning-type friction as the main prototype (Popov and Gray, 2012), such models typically postulate that the elastic energy landscape is wiggly and associate dissipation with snap-through instabilities, which typically accompany quasi-static driving in systems of this type (Puglisi and Truskinovsky, 2005).

The development of the tensorial version of such 'purely elastic' models was inspired by the pioneering insights of Ericksen (1970, 1977), which were almost immediately endorsed by Parry (1976) and Hill (1979). The MTM represents an important step in the development of this class of models, offering their geometrically-exact finite-strain generalization. Its main achievement is in turning prototypical schemes into fully comprehensive and technologically relevant engineering tools. In the spirit of continuum crystal plasticity, the MTM links plastic deformation with crystallographically-specific valleys in the elastic-energy landscape, however, it replaces the 'flat' valleys of the CP theory by 'periodically modulated' ones. Instead of being postulated, these valleys emerge in the MTM as natural elements of the globally-periodic configurational energy landscape constructed to respect the tensorial symmetries of lattice-invariant shears, see Ericksen (1980), Boyer (1989), Folkins (1991), Wang et al. (1993), Waal (1990), Parry (1976, 1977, 1998), Pitteri (1984a), Conti and Zanzotto (2004), Pitteri and Zanzotto (2002).

The downscaling from macro to meso scale is accompanied in the MTM by two types of discretization. The first one concerns the *configurational space* of strain tensors. It involves the quantization of plastic deformation, which is natural in view of the implied periodicity of the associated Landau-type elastic energy density characterized by an infinite number of equivalent energy wells. The second concerns the *physical space* and amounts to the representation of an inhomogeneously deformed macroscopic body as a collection of homogeneously deformed mesoscopic elements. This step is formally necessary as a regularization since the configurational nonconvexity of the energy density creates an unphysical degeneracy (Fonseca, 1987).

Note that none of the emerging discretization scales is a part of classical continuum CP, which can then be viewed as a fully macroscopic extension of the MTM. The implied coarse-graining in CP comes with the loss of information, in particular, the short-range interactions involved in topological transitions have to be brought through *ad hoc* phenomenological assumptions prescribing, for instance, the rate of dislocation nucleation and of other dislocation reactions. Still, despite the underlined profound differences between CP and the MTM, we attempt in this paper to build a new conceptual bridge between the two theories.

Our main idea is the re-introduction into the MTM of the crucial concept of plastic deformation. As we have already mentioned, in its original formulation, the MTM had the guise of a 'purely elastic' theory (Baggio et al., 2023a). While this may create an impression that the notion of plastic strain is completely foreign to the MTM, the concept has actually already appeared explicitly in the scalar version of the MTM in the form of an integer-valued (quantized) order parameter (Salman and Truskinovsky, 2011, 2012; Zhang et al., 2020a). Interestingly, the reason for its introduction in such a restricted setting was not conceptual but technical, as it enabled the explicit reduction of the description of plastic flow to a simple integer-valued automaton.

Here we generalize the idea of quantized plastic strain, implicit in Salman and Truskinovsky (2011, 2012), Zhang et al. (2020a), by placing it in the fully tensorial MTM framework. We show that in the finite-strain setting, plastic strain can be naturally associated with a locally-defined integer-valued matrix, whose role is to select one among the infinitely many equivalent wells of the globally periodic constitutive energy landscape. In this perspective, crystal plasticity emerges as a physical theory where the order parameter is a matrix-valued spin variable. The proposed re-formulation of the MTM can be then viewed as a transition from the soft-spin, 'purely elastic' description, to the hard-spin, elasto-plastic description.

By enabling explicit access to plastic strain in a DE-based model, the proposed re-formulation of the MTM opens the possibility to follow the history of quantized lattice-invariant deformations, which remains hidden behind the smoothness of macroscopic plastic flows. The reference to the discreteness of slip also creates a new link between the molecular representation of lattice-invariant

deformations and the engineering, continuum level, description of plastic fluctuations in terms of macroscopically observable quantities.

The most important technical advantage of introducing the explicit distinction between elastic and plastic contributions to deformation is the possibility to effectively separate (in the case of quasi-static driving) the *continuum* elasticity problem from the *discrete* plasticity problem. We show that when such a separation is complete, the well-posed elastic problem can be solved 'on the fly', allowing one to relegate the evolution of the plastic strain to a tensorial integer-valued automaton. In other words, in the resulting 'condensed' description, see Junker and Hackl (2013), Carstensen et al. (2008), Jezdan et al. (2023), the dissipation is effectively removed from the continuous problem, which reduces to smooth energy minimization, while remaining associated with a discrete sequence of discontinuous elastic instabilities, each of which is accompanied by a finite energy drop, representing quantized advance of plastic strain. The associated updates of the automaton mimic discontinuous elastic-branch-switching events related, for instance, to collective bond breaking and attendant bond reforming.

It is important to point out that, outside the simplest scalar setting, the numerical algorithm for the solution of the 'condensed' MTM problem can be interpreted only as a *quasi-automaton*. While, indeed, it describes a sequence of load-driven updates of quantized plastic variables, each of those updates necessarily contains an embedded elastic energy-minimization step. Behind the incomplete separability of the elastic and plastic problems lies the geometric nonlinearity of the elastic problem, which cannot be neglected due to the ubiquitous presence in elastoplastic flows of large rotations, see Baggio et al. (2023a,b), Dafalias (1998), Arminjon and Imbault (2021), Boyce et al. (1989), Levitas (1998), Fathallah et al. (2019).

Still, we show that in the new version of the MTM, the elastic energy density can be chosen in such a way that the solution of the elastic problem is practically straightforward even if it cannot be expressed in terms of an explicit 'elastic propagator' as in the scalar problem (Salman and Truskinovsky, 2011, 2012; Zhang et al., 2020a). Therefore, even in the absence of complete separation of the elastic and plastic problems, a detailed estimate of the algorithmic complexity of the new approach suggests up to two orders of magnitude reduction of the computational time vis-a-vis the original 'purely elastic' approach. As we show, significant acceleration potential of the proposed re-formulation of the MTM lies in the possibility to perform only local elastic adjustments in response to discrete plastic updates.

To illustrate the effectiveness of the elasto-plastic version of the MTM, we present in this paper a detailed case study of the emergence of plastic yield in (almost) pristine 2D square crystals subjected to homogeneous loading in a hard device. We present a series of numerical experiments designed to reveal the aspects of crystal plasticity that are beyond reach for the classical CP approach and our main interest is in the critical nature of the emerging plastic flow. The latter is revealed through a peculiar statistical signature of plastic fluctuations representing dislocation avalanches. Specifically, our study provides a definitive evidence for the non-Gaussian character of plastic flows with the emergence of spatial and temporal scaling.

In particular, we show that the statistics of the intermittent energy-dissipating dislocational avalanches accompanying plastic yield exhibits a power-law tail with a critical exponent matching the value predicted by some theoretical considerations and independently observed in discrete-dislocation-dynamics simulations. We also show that the spatial-distribution of slip zones is characterized by a non-integer fractal dimension, which, again, closely matches the value anticipated by the general theory. The computed relation between the macroscopic stress and macroscopic plastic strain is found to be well approximated by the empirical Johnson-Cook strain-hardening scaling law with a hardening exponent remarkably close to the one found experimentally for a material with similar parameters.

The paper is organized as follows. In Section 2, we motivate our approach by considering an oversimplified zero-dimensional model. The detailed fully analytical study of this model makes the main ideas of the subsequent development explicit and transparent. The 2D version of the MTM, containing continuum elastic and discrete plastic strain measures, is formulated in Section 3, where we also address various aspects of the numerical implementation of the model. In Section 4 we present a case study of a fluctuating plastic flow in a model crystal and rationalize the emerging scale-free statistics. Our results are summarized in Section 5. Several appendixes contain discussions of a more technical nature.

2. Preliminaries

Continuum plasticity. The standard assumption in finite-strain plasticity is that the compatible deformation gradient $\mathbf{F} = \nabla \mathbf{y}^\top$ corresponding to the total deformation $\mathbf{y}(\mathbf{x})$ can be multiplicatively decomposed into a product of (potentially incompatible) elastic, $\mathbf{F}_e$, and plastic, $\mathbf{F}_p$, contributions, such that, see Clayton (2010), Reina and Conti (2014), Roters et al. (2010),

$$\mathbf{F} = \mathbf{F}_e \mathbf{F}_p.$$

The objective elastic energy density per reference volume can be then written in the form $\psi = \psi(\mathbf{C}_e)$, where $\mathbf{C}_e = \mathbf{F}_e^\top \mathbf{F}_e$ is the elastic metric tensor. If the loading is fixed and the plastic distortion $\mathbf{F}_p$ is known, the deformation $\mathbf{y}(\mathbf{x})$ can be found by solving the equilibrium equations

$$\nabla \cdot \mathbf{P}^\top = 0,$$

where $\mathbf{P} = 2\mathbf{F}_e \frac{\partial \psi}{\partial \mathbf{C}_e} \mathbf{F}_p^{-\top}$ is the (first) Piola–Kirchhoff stress. From the equilibrium equations complemented by the appropriate boundary conditions one obtains the solution of the 'elastic' part of the problem (Simo and Thomas, 2010; Lubliner, 2008; Han and Reddy, 2012; Schröder and Hackl, 2013).

The 'plastic' problem, which reduces to finding $\mathbf{F}_p$, is solved concurrently with the 'elastic' problem. The corresponding equations are usually formulated in incremental form and involve constitutive assumptions, which identify plastic 'mechanisms' while also

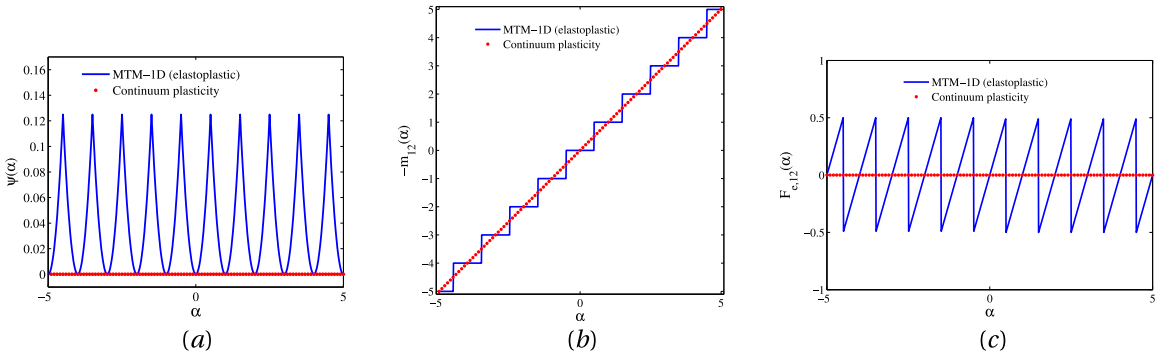

Fig. 1. Schematic comparison of the MTM (blue) and the CP (red) based response under one-parametric simple shear loading in a hard device: (a) energy density, (b) plastic distortion $F_{p,12} = -m_{12}$, (c) elastic distortion.

specifying the corresponding yield conditions, flow rules and hardening laws. The only fundamental constraint imposed on such phenomenological assumptions is the incremental condition of the overall dissipativity of plastic deformation, $\mathbf{tr}(\mathbf{P}^{\top}\mathbf{F}_e\dot{\mathbf{F}}_p) \geq 0$, see Roters et al. (2010), McDowell (2018).

To better understand the implied separation of elastic and plastic problems, we observe that in such a continuum theory the elastic energy density can be written in the form

$$\psi = \psi(\mathbf{F}\mathbf{F}_p^{-1}).$$

This representation suggests that if $\mathbf{F}_p$ is compatible, the distortions with $\mathbf{F} = \mathbf{F}_p$ appear as elastically 'soft' modes. In other words, the elastic energy density of continuum CP would be degenerate along such tensorial directions. The associated 'plastic mechanisms', which can be prescribed by the ansatzes imposed on $\mathbf{F}_p$, are usually indeed chosen to be compatible, crystallographically-specific simple shears (rank-one directions in the space of deformation gradients), see (Asaro, 1983; Gurtin, 2000; McHugh, 2004).

To ensure that the plastic flow along the implied flat energy valleys, cutting through the configurational elastic energy landscape, is dissipative, continuum theories of the CP type introduce effective (dry) friction operating along the valleys and encapsulated in the corresponding yield thresholds and flow rules. Those are chosen to be necessarily compatible with the dissipativity inequality, see Gurtin (2000), Rice (1971), Mielke (2003), Petryk (2005), Svendsen and Bargmann (2010).

Ideas behind the MTM. To avoid redundant CP phenomenology without giving up the macroscopic concepts of stress and strain, the MTM approach transforms the rigid constitutive assumptions of CP regarding the 'plastic mechanisms' into constraints of a 'soft' nature emerging naturally from the geometrically necessary structural properties of the configurational energy landscape $\psi(\mathbf{C})$.

Moreover, in its 'purely elastic' form the MTM anticipates that the analogues of the conventional concepts of yield surface and flow rule are generated automatically after the configurational landscape is prescribed. In particular, it interprets the yield surface as an extended corridor in the configurational space where elastic instabilities in individual elastic elements are activated as the system is driven away from an energy well. Similarly, it views the flow rule as a post-instability response aimed at the stabilization of the individual destabilized elements in new energy wells. In the MTM, it is also connoted that such a stabilization is guided by an overdamped dynamics of the viscous type. In the case of quasi-static driving, the latter takes the form of continuous local energy minimization with occasional discontinuous transitions between the neighboring energy wells. It is also anticipated that the geometrically necessary structure of the configurational energy landscape ensures that all such discontinuous transitions are accompanied by energy loss. This means, in particular, that the dissipativity condition is always satisfied, despite the fact that in a quasi-static setting the effective (normalized) viscosity is effectively equal to zero.

As far as the inner structure of the energy valleys is concerned, the MTM approach effectively assumes that the 'frictional' dissipation mechanisms, operating at a macro-scale, can be modeled by the periodic modulation of the elastic energy landscape inside the valleys. Such a modulation is then viewed as a signature of the meso-scale description, which disappears in the process of macroscopic coarse-graining (Mielke and Truskinovsky, 2012).

The first step in the implementation of all these ideas is to specify the configurational energy landscape $\psi(\mathbf{C})$, representing, in a geometrically precise way, the relevant lattice-invariant shears. The corresponding quantized strains would then be represented by the equivalent energy minima in such a tensorial landscape. If the latter is constructed to respect the crystallographic symmetry of the crystal lattice, the modulated energy valleys, imitating 'plastic mechanisms', would appear automatically, and plastic dissipation would emerge as a sheer consequence of energy minimization (Baggio et al., 2019).

Quantized plastic strain. To illustrate in the simplest form the idea that the introduction of a periodically modulated valley inside the configurational energy landscape can lead to the description of lattice-invariant shears, we now consider the elementary shear deformation path

$$\mathbf{F} = \begin{bmatrix} 1 & \alpha \\ 0 & 1 \end{bmatrix}, \tag{2.1}$$

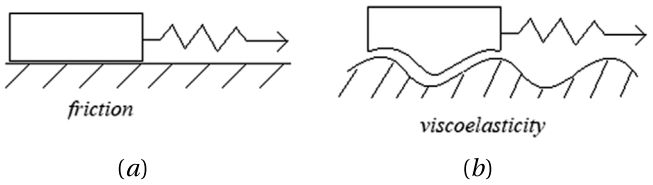

Fig. 2. Schematic representation of a zero-dimensional model as it operates at the macro-scale (a) together with its analogue operating at the meso-scale (b).

where α will be interpreted as a loading parameter (in a hard loading device). Suppose that the path (2.1) extends along the floor of a valley inside the energy landscape $\psi(\mathbf{F})$, which would correspond in the CP framework to a 'plastic mechanism'. While in CP the elastic energy along such a path would be identically equal to zero, see the red line $\psi(\mathbf{F}(\alpha)) \equiv 0$ in Fig. 1(a), in the MTM we postulate that the energy $\psi(\mathbf{F}(\alpha))$ is periodic. For simplicity we can further assume that the corresponding one-dimensional energy landscape is described by the piecewise-quadratic function

$$\psi(\mathbf{F}(\alpha)) = \frac{\mu}{2}\left[\alpha - \left\lfloor |\alpha| + \frac{1}{2}\right\rfloor \mathrm{sgn}(\alpha)\right]^2, \tag{2.2}$$

where $\lfloor\cdot\rfloor$ is the 'floor' function (the greatest integer less than or equal to the argument) and μ is the effective shear modulus. Note that while in the CP framework we could assume that all the distortions $\psi(\mathbf{F}(\alpha))$ are purely plastic, in the MTM framework the distinction between the elastic and the plastic distortion becomes more subtle.

In view of the inherent discreteness of plastic deformation, the natural choice of the meso-scale plastic distortion would be the integer-valued matrix

$$\mathbf{m}(\alpha) = \begin{bmatrix} 1 & -\left\lfloor |\alpha| + \frac{1}{2}\right\rfloor \mathrm{sgn}(\alpha) \\ 0 & 1 \end{bmatrix}. \tag{2.3}$$

Here we implicitly assume that $\mathbf{F}_p^{-1}(\alpha) = \mathbf{m}(\alpha)$. In other words, the meso-scale plastic distortion would correspond to the blue line in Fig. 1(b), which is different from the red line in Fig. 1(b), representing the conventional macro-scale assumption of the CP approach. One can see that the meso-scale plastic distortion exhibits a "staircase" structure, where vertical segments, indicating discrete integer-valued slips, correspond to quantized advances of plastic deformation, while the horizontal segments describe the complementary, purely elastic, deformation. Furthermore, while in the CP approach we have $\mathbf{F}_e(\alpha) \equiv 0$ (red horizontal line in Fig. 1(c)), our quantized assumption (2.3) combined with the multiplicative decomposition $\mathbf{F}_e(\alpha) = \mathbf{F}(\alpha)\mathbf{m}(\alpha)$, gives a different expression for the elastic distortion (blue zigzag line in Fig. 1(c)):

$$\mathbf{F}_e(\alpha) = \begin{bmatrix} 1 & \alpha - \left\lfloor |\alpha| + \frac{1}{2}\right\rfloor \mathrm{sgn}(\alpha) \\ 0 & 1 \end{bmatrix} \tag{2.4}$$

As we see, an elastic distortion, associated with the activation of a meso-scopic 'plastic mechanism', is described by a piece-wise continuous function oscillating around zero.

This simple example suggests that the quantized increments of plastic distortion occur when the driven system reaches the boundaries of one of the equivalent elastic domains, each containing a replica of one elastic energy well. Inside each of such domains the mechanical response is purely elastic and the transitions between neighboring domains can be viewed as 'elastic instabilities'. The corresponding strain threshold can be interpreted as a simplistic 'yield criterion' and since the system can advance only between the neighboring domains, the associated (quantized) advances of plastic strain are then governed by an equally oversimplified 'flow rule'.

Zero-dimensional model. The above discussion of a simple example can serve as an illustration of the idea of periodically modulated valleys in the MTM. However, such a discussion remains largely kinematic as no equilibrium equations are involved, and since no dissipation is associated with 'elastic instabilities'. To address these and other related issues, we need to augment our model mechanically. At the same time it should be simplified geometrically if the goal is to maintain the same level of analytical transparency. With this idea in view we now consider another simple example explaining how in the MTM the discrete (quantized) evolution of plastic strain can be driven externally. We use the same example to also explain why such an evolution is caused by elastic instabilities, which are necessarily dissipative.

The zero-dimensional toy model which serves our purposes was first proposed by L. Prandtl (Prandtl, 1928; Popov and Gray, 2012; Abeyaratne et al., 1996; Choksi et al., 1999; Heslot et al., 1994), see Fig. 2. It provides an elementary representation of a *depinning* phenomenon dealing with an elastic object (manifold) being dragged along a modulated background; the latter allows for a large number of equilibrium configurations where the elastic manifold can be pinned (Fisher, 1998; Kardar, 1998). Prandtl was the first to realize that depinning could be the right qualitative (but not necessarily quantitative) metaphor for crystal plasticity, where the manifold is a network of elastically linked defects, the role of modulations is played by the system of lattice-invariant shears and dragging is ensured by the applied loads.

Below we use this prototypical model to illustrate the fact that the dry-friction-type dissipation on a flat surface can emerge as a homogenized description of an externally driven viscous-type dynamics on a periodically modulated surface, the latter being

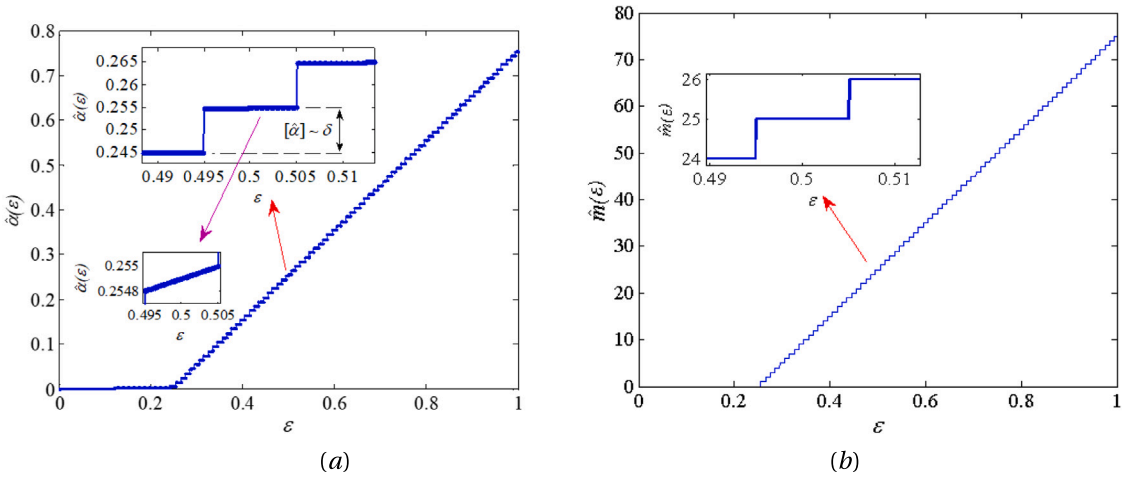

Fig. 3. 'Equilibrium' responses of (a) total strain, $\hat{\alpha}(\varepsilon)$, and (b) plastic strain, $\hat{m}(\varepsilon)$, produced by the zero-dimensional model for $k/E = 1/2$, $\delta = 0.01, \nu \to 0$.

exemplified by the depinning phenomenon. More broadly, our goal is to show that the classical ideally plastic dissipative response, described in CP by a homogeneous dissipative function of degree one, can be viewed as an averaged description of an MTM-type response with viscoelastic (quadratic) dissipation. Our analysis shows that behind the nontrivial nature of such coarse graining lies a cascade of sub-critical elastic instabilities leading to fast and abrupt embedded rearrangements, which remain dissipative even in the case of quasi-static driving (Puglisi and Truskinovsky, 2005; Mielke and Truskinovsky, 2012).

The model shown in Fig. 2(b) is characterized by the energy

$$f(\varepsilon, \alpha) = -k\delta\psi\left(\frac{\alpha}{\delta}\right) + \frac{E}{2}(\alpha - \varepsilon)^2. \tag{2.5}$$

Here the first term on the right represents the MTM-type energy landscape presumed to be operative inside the (periodically modulated) plastic energy valley. The second term describes the elasticity of the environment, operative outside such a valley. One can view this term as a description of the elastic coupling between the 'plastic mechanism' and the loading device.

In view of this interpretation, the variable α emerges as the representation of plastic distortion, while the role of the loading parameter is played by ε. For simplicity, we assume that the periodic potential ψ is piecewise quadratic and write it first in the form $\psi = -\frac{1}{2}(z - m)^2$, where m is the integer-valued parameter. To ensure the periodicity of ψ and to remain in the 'purely elastic' setting, we complement the definition by the assumption that $m = \left\lfloor |z| + \frac{1}{2} \right\rfloor \mathrm{sgn}(z)$.

The resulting model is then characterized by the energy

$$\psi(z) = 1 - \frac{1}{2}\left[z - \left\lfloor |z| + \frac{1}{2} \right\rfloor \mathrm{sgn}(z)\right]^2. \tag{2.6}$$

We observe that the quantized variable m selects at a given z a particular (energy minimizing) parabola, however, being enslaved to z, it does not play an independent role in the response of the system. The implied adiabatic elimination of the m-type variable represents a defining feature of the current version of the MTM, where plastic strain is not present explicitly.

To complete the introduction of the Prandtl model, we should mention that the small parameter δ is a measure of discreteness, which points to the meso-scopic nature of this model. We show below that the analogue of the macro-scale CP model emerges from (2.5) in the limit $\delta \to 0$; the remaining parameters k and E characterize in the ensuing coarse-grained continuum model the yield stress and the elastic potential.

Suppose next that the dynamics in the system with the energy (2.5), (2.6) is overdamped-viscous and is described by the gradient-flow type kinetic equation

$$\dot{\alpha} = -\gamma \partial f(\varepsilon, \alpha)/\partial\alpha,$$

where γ is a measure of the relaxation time. We also assume that the system is driven in a hard device with a rate of

$$\dot{\varepsilon} = v > 0.$$

In the quasi-static limit,

$$\nu = v/\gamma \to 0,$$

the energy in such a system is locally minimized almost always and we can use the equilibrium condition $\partial f(\varepsilon, \alpha)/\partial\alpha = 0$ to define the locus of the equilibrium response $\hat{\alpha}(\varepsilon)$. Assuming that $\delta \ll k/E$ (strong pinning condition) we obtain an explicit formula:

$$\hat{\alpha}(\varepsilon) = \frac{k\delta}{k + E\delta}\max\left[0, \min\left(\left\lfloor \frac{\varepsilon}{\delta} \right\rfloor, \left\lceil \frac{\varepsilon}{\delta} - \frac{1}{2} - \frac{1}{2}\frac{k}{E\delta} \right\rceil\right)\right] + \frac{E\delta\varepsilon}{k + E\delta}. \tag{2.7}$$

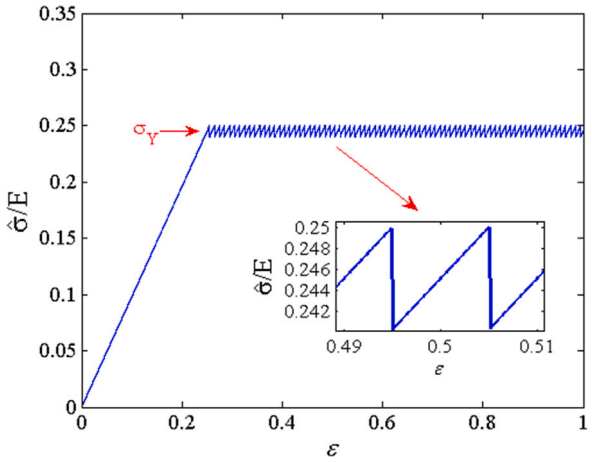

Fig. 4. Macroscopic stress–strain relation $\hat{\sigma}(\varepsilon)$ in the zero-dimensional model with $k/E = 1/2, \delta = 0.01, \nu \to 0$.

The computed elastic response, shown in Fig. 3(a), is characterized by a prolonged initial elastic range where the system remains in the original energy-well and where the elastic strain $\hat{\alpha}$ changes with ε linearly. The subsequent evolution is a repetition of the same pattern: a succession of linear segments, signaling that the system remains inside the same energy well, interrupted by the transitions to the neighboring wells occurring during the short increments of the loading 'time' ε, which scale with the small parameter δ.

We can now argue that the loading level when the system reaches the boundary of the original energy-well indicates the beginning of plastic yield and that the corresponding (identical) jump events can be associated with plastic slips. If we now reconstruct the evolution of the integer-valued variable m, we obtain:

$$\hat{m}(\varepsilon) = \max\left[0, \min\left(\left\lfloor \frac{\varepsilon}{\delta} \right\rfloor, \left\lceil \frac{\varepsilon}{\delta} - \frac{1}{2} - \frac{1}{2}\frac{k}{E\delta} \right\rceil\right)\right]. \tag{2.8}$$

The emerging response $\hat{m}(\varepsilon)$, illustrated in Fig. 3(b), suggests that the variable m can be interpreted as the integer-valued measure of plastic strain. Indeed, the prolonged pre-yield elastic range is characterized by the condition $\hat{m} = 0$, while after the yield we observe the repeating 'staircase'-type pattern of elastic horizontal steps and (almost) discontinuous transitions of the type $\hat{m} \to \hat{m} + 1$. The conceptual problem with this interpretation is that the variable m remains implicit while both the elastic and the plastic phases of the response are still fully characterized by a single strain variable α. Before we turn the variable m into an independent 'player' in the model, it is instructive to rationalize the obtained elasto-plastic response in energetic terms.

We first recapitulate that the quasi-static evolution of our 'purely elastic' system takes place at the slow time scale of the loading, $\tau = vt$. This slow evolution is periodically interrupted by the fast events occurring at the relaxational time scale t. During the slow (elastic, equilibrium) stages of the evolution, the elastic strain $\hat{\alpha}$ varies continuously on the scale τ, while the system stays on the same equilibrium branch of the elastic response. On the other hand, during the fast (plastic, nonequilibrium) stages of the evolution, the elastic strain $\hat{\alpha}(\varepsilon)$ changes on the scale t, and the system transitions between neighboring branches of elastic equilibria. In the quasi-static limit $\nu \to 0$ such transitions can be viewed as happening instantaneously and we can associate them with (over-simplistic) plastic avalanches. In this limit, plastic avalanches are accompanied by the discontinuities of both the strain and the energy, taking place at a fixed value of the loading parameter. The periodically-spaced stress drops can be seen on the macroscopic stress–strain curve $\hat{\sigma}(\varepsilon) = d\hat{f}/d\varepsilon$, shown in Fig. 4. The energy jumps are also clearly visible on the macroscopic energy-strain curve $\hat{f}(\varepsilon) = f(\varepsilon, \hat{\alpha}(\varepsilon))$, shown in Fig. 5. We note that the formally computed area under the graph $\hat{\sigma}(\varepsilon)$ has nothing to do with the elastic energy stored in the system, as the measure-valued fluctuations of stress associated with abrupt drops of energy $\hat{f}(\varepsilon)$ would not be properly accounted for in such a naïve computation, see Puglisi and Truskinovsky (2005) for more details.

It is clear, though, that during the elastic stages of the deformation all the work of the loading is indeed stored in the system, as the dissipation associated with the phenomena occurring in slow time is absent in the limit $\nu \to 0$. Instead, the plastic-correction events, occurring in fast time, remain dissipative, notwithstanding the quasi-static nature of the loading, as can be seen clearly from the plot of the energy $\hat{f}(\varepsilon)$ in Fig. 5. One therefore finds that after the yield stress is reached the energy-strain relation is punctuated by abrupt energy drops, attesting to the fact that the associated branch-switching transitions are dissipative. While in our overdamped model the released energy simply disappears, in more realistic systems it is either converted to lattice-scale vibrations, see Efendiev and Truskinovsky (2010), or emitted in the form of acoustic waves, see Weiss et al. (2021).

The amount of energy dissipated in each of the elastic branch-switching events is

$$-\int (\partial f/\partial\alpha)\dot{\alpha}dt = -[\![\hat{f}]\!] \geq 0, \tag{2.9}$$

where we introduced the notation $[\![A]\!] = A_+ - A_-$ for the difference between the values after and before the jump (fast event). We emphasize that the integration in (2.9) is over the duration of the transition in fast time and the integral is different from zero in the limit $\nu \to 0$ because as duration tends to zero, the rate of deformation tends to infinity.

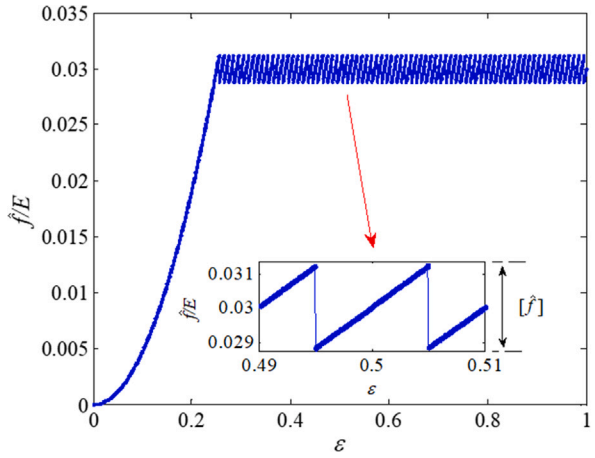

Fig. 5. Macroscopic energy-strain relation $\hat{f}(\varepsilon)$ in the zero-dimensional model with $k/E = 1/2, \delta = 0.01, \nu \to 0$.

As we see, the system experiences a cascade of dissipative events, separated by regularly spaced dissipation-free elastic stages. The total dissipation is then $-\sum[\![\hat{f}]\!]$ and it is clear that it depends not on the rate of loading but only on the number of occurred jumps. This suggests that in the continuum limit

$$\delta \to 0$$

the resultant continuous dissipation will be rate-independent. Indeed, in this limit, which symbolizes the transition from meso to macro scale, the magnitudes of the jumps tend to zero while, due to a particular choice of the scaling in our zero-dimensional model, their number increases indefinitely so that the total dissipation remains finite.

More specifically, one can show (Puglisi and Truskinovsky, 2005) that the limiting continuous dissipative potential is described by a homogeneous function of degree one:

$$D = \sigma_Y|\dot{\hat{\alpha}}|,$$

where σ_Y is the effective 'yield stress'. To compute the value of σ_Y we observe that under the assumption that $\delta \ll k/E$, each plastic avalanche produces a strain jump with the $\delta \to 0$ asymptotics $[\![\hat{\alpha}]\!] = \hat{\alpha}^{(m+1)} - \hat{\alpha}^{(m)} \sim \delta$. To evaluate the magnitude of the corresponding energy drops we write $[\![f(\varepsilon,\hat{\alpha})]\!] = -k\delta[\![\psi(\hat{\alpha}/\delta)]\!] + \frac{E}{2}[\![(\hat{\alpha}-\varepsilon)^2]\!]$ where $\frac{E}{2}[\![(\hat{\alpha}-\varepsilon)^2]\!] \sim -\frac{k}{2}\delta$ and $-k\delta[\![\psi(\hat{\alpha}/\delta)]\!] \sim -\frac{1}{2}E\delta^2$. Therefore $[\![f(\varepsilon,\alpha_0)]\!] \sim -\frac{1}{2}k\delta$ and we finally obtain an explicit relation for the effective yield stress:

$$\sigma_Y = -\lim_{\delta\to 0}\frac{[\![f(\varepsilon,\hat{\alpha})]\!]}{[\![\hat{\alpha}]\!]} = \frac{1}{2}k. \tag{2.10}$$

To summarize, the zero-dimensional model of Prandtl conveys the main ideas behind the 'purely elastic' version of the MTM and adequately reproduces the main targeted empirics. Thus, according to this toy model, an extended range of initial purely elastic response ends with the emergence of plastic yield. The latter reveals itself through the periodic fluctuation of the stress around the yield value σ_Y. The fluctuations take the form of a repeating pattern of elastic 'prediction' segments, representing continuous deformation inside one energy well (with ε changing at fixed m), interrupted by the abrupt drops, representing plastic 'correction' events (singular quantized advances of $\hat{m}$ at fixed ε).

While the obtained fluctuation structure is still hardly realistic (trivial statistics of plastic avalanches, no intermittency), it is clear that the model captures the fundamentals of rate-independent plasticity (elastic range, plastic yield, presence of fast motions embedded in the otherwise quasi-static evolution, etc.). Even the so-called nucleation peak, a quasi-brittle event (avalanche) associated with the initial massive slip nucleation in a pristine crystal, can be easily recovered already in a one-dimensional generalization of this zero-dimensional model (Truskinovsky and Vainchtein, 2004). This does not mean, of course, that such schematic a representation of crystal plasticity is adequate. The task of implementing the same basic ideas but in the full tensorial setting and in arbitrary dimension with the goal of comprehesive description of plastic fluctuations has been accomplished through the development of the 'purely elastic' version of the MTM (Baggio et al., 2019, 2023a; Salman et al., 2021; Baggio et al., 2023b).

Here we attempt to go a bit further. The main ideas of the proposed re-formulation of the MTM can be explained already at the level of the zero-dimensional model. As we have previously mentioned, the elastic and plastic problems in the original Prandtl model are not separated and although in the above discussion we referred to the variable m as describing plastic slip, in such 'purely elastic' a model the variable m did not play an essential role. That is why we consider below another version of the Prandtl model, where the elastic and the plastic problems are fully separated, and where the variable m acquires independent significance. The main advantage of such a reformulation is that the elastic field can be minimized out while the 'condensed' description of plastic response in terms of the field m alone can be reduced to an integer-valued discrete automaton.

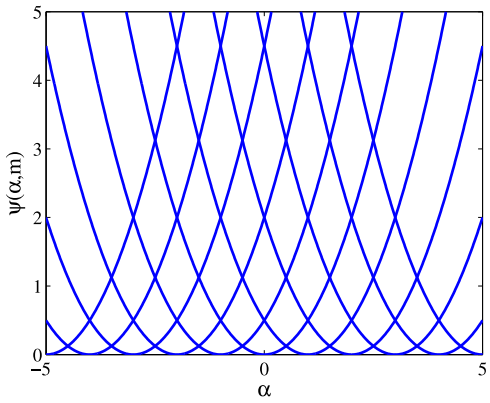

Fig. 6. Schematic representation of the multivalued function $\psi(\alpha)$.

Discrete automaton representation. In the zero-dimensional toy model described above the elastic and the plastic problems could not be addressed independently. Although we formally introduced in this model the quantized plastic strain, the variable m potentially representing $\mathbf{F}_p$, could be effectively enslaved to the variable α, representing the elasto-plastic strain, which we can still denote by $\mathbf{F}_e$, given that in this zero-dimensional setting the role of the deformation gradient $\mathbf{F}$ is played by the loading parameter ε. Therefore, in such a representation we are essentially dealing with a quasistatically driven nonlinear-elastic system exhibiting a regular succession of internal snap-through instabilities.

The goal of the proposed reformulation of the Prandtl model is to give the plastic distortion m full autonomy. To circumvent the 'purely elastic' structure of the original Prandtl model, we now abandon the idea of performing (adiabatic) elimination of the plastic strain m. Instead, we follow the general approach of classical continuum CP and interpret the integer-valued parameter m as an independent variable. Staying within the same piecewise-quadratic paradigm as before in describing elasticity, we can introduce the two-parametric energy density

$$\psi(\alpha, m) = -\frac{1}{2}\left(\frac{\alpha - m}{\delta}\right)^2, \tag{2.11}$$

where now the continuous variable '$\alpha(m,\varepsilon) - m$' represents the elastic strain $\mathbf{F}_e$, and the integer-valued variable m represents the plastic strain $\mathbf{F}_p$. Since the two variables, α and m, are now considered independent, the elastic energy density dependence on α becomes formally multivalued, as it is now represented by an infinite number of discrete branches parametrized by the value of the variable m, see Fig. 6. However, the nonlinearity of the problem and the single-valuedness of the energy can be recovered if we place an additional constraint, namely, that the elastic strain is confined between the limits

$$m - 1/2 \le \alpha - m \le m + 1/2. \tag{2.12}$$

These inequalities can be interpreted as defining the 'elastic domain' corresponding to a given value of m. The whole range of possible values of α can be then viewed as being tessellated by the infinite number of equivalent 'elastic domains' of this type, representing the periodicity domains of the elastic energy. In other words, with the inequalities (2.12) imposed, the model becomes again 'purely elastic' as the plastic strain variable m is then effectively minimized out. As we show in what follows, the re-formulation of the MTM proposed here anticipates that the analogues of the inequalities (2.12) can be omitted at the stage of elastic 'prediction' and it would be sufficient to implement them only at the stage of 'elasto-plastic' correction. This basic idea is illustrated below in the framework of our zero-dimensional model.

Observe that with inequalities (2.12) suppressed, the equilibrium elastic response $\alpha(m,\varepsilon)$ at a given value of m can be found (in the model with the energy (2.5), (2.11)) explicitly, as:

$$\alpha(m,\varepsilon) = \frac{km + E\delta\varepsilon}{k + E\delta}. \tag{2.13}$$

In other words, the assumption of linear elasticity at a fixed m allows one to minimize out the variable α and opens the possibility of obtaining a 'condensed' description in terms of the measure of plastic strain m only. However, we reiterate that since the resulting elastic strain, $\alpha(m,\varepsilon) - m$, may not be located inside the corresponding 'elastic domain' $(m - 1/2, m + 1/2)$, the expression (2.13) does not represent the solution of the elastic problem and, given the value of the loading parameter ε, can be at most interpreted as an elastic prediction.

Saying it differently, if the value of m at the given ε agrees with the 'equilibrium' expression $\hat{m}(\varepsilon)$ given in (2.8), then the condition (2.12) is automatically satisfied and no elasto-plastic correction is necessary. If, however, the predicted elastic strain at the given m and ε is located outside the corresponding 'elastic domain', the configuration (2.13) should be rendered unstable, which

means that an elasto-plastic correction should be performed with the idea that as a result of such correction the corresponding value $\hat{m}(\varepsilon)$ is attained. More specifically, since in this case the effective 'yield condition' (2.12) is violated, the value of the plastic strain m must undergo a quantum update,

$$m \to m \pm 1,$$

one or several times. An elementary update of this type (elementary plastic correction) can be then interpreted as the action of a primitive 'flow rule'. After an update is completed, the equilibrium elastic problem for α can be solved again producing an elastic correction. The implied iterative process can continue until the plastic strain m is finally compatible with the 'equilibrium' response $\hat{m}(\varepsilon)$.

The main advantage of our simplified description of elastic response inside each 'elasticity domain' is that the numerical algorithm alluded above can be formulated without any reference to the variable α, which, given that the equilibrium equation $\partial f/\partial\alpha = 0$ is solvable explicitly, could be thus considered as effectively eliminated. The equations governing the evolution of the plastic strain m in the resulting 'condensed' problem reduce to a discrete dynamical system that can be formulated as an integer-valued automaton:

$$\varepsilon \to \varepsilon + \Delta\varepsilon \quad \Rightarrow m \to m + \Delta m, \tag{2.14}$$

where

$$\Delta m = \begin{cases} 0, & \frac{\varepsilon}{\delta} - \frac{1}{2} - \frac{1}{2}\frac{k}{E\delta} + 1 < 1 \\ -1, & 1 \le \frac{\varepsilon}{\delta} - \frac{1}{2} - \frac{1}{2}\frac{k}{E\delta} + 1 \le m \\ 1, & \frac{\varepsilon}{\delta} - \frac{1}{2} - \frac{1}{2}\frac{k}{E\delta} > m \end{cases}. \tag{2.15}$$

Generically, the discrete mapping (2.14), (2.15) performs the update from m to $m + \Delta m$ in response to the load increment $\Delta\varepsilon$, however, at a given value of ε, depending on the value of $\Delta\varepsilon$, such an update of m may or may not be warranted. Indeed, the quantized variable m is updated by an elementary correction step ± 1 only if one of the thresholds in (2.12) is violated. In the 'condensed' formulation (2.15) the solution of the elastic problem is, of course, hidden behind the expressions for the thresholds. Note that in the limit $\Delta\varepsilon \to 0$ (and in our numerical experiments, with the automaton in (2.14), (2.15), and the parameter values given in Fig. 3, already for $\Delta\varepsilon < 10^{-4}$), no elastic correction is ever needed and the automaton in (2.14), (2.15) reproduces exactly the equilibrium response given in (2.8).

Comparison of the two prototypical zero-dimensional models discussed above suggests that, despite the differences in appearance, the discrete dynamics of the plastic strain m under sufficiently small increments of the loading parameter is basically the same in the two models. The main advantage of the introduction of the simple multi-valued elastic energy is that the elastic problem becomes fully separated and could be solved implicitly 'on the fly'. Then, under the assumption that the loading ε changs quasistatically, the evolution of plastic strain in the 'condensed' problem reduces to an integer-valued automaton whose structure was not apparent in the 'purely elastic' setting of Prandtl. The complexity of the nonlinear evolution problem in the Prandtl model is then relegated to a simple integer-valued discrete dynamical system governing the dynamics of a quantized plastic variable. The ensuing automaton description is fully adequate and in the limit of slow driving it perfectly recovers the staircase-like piece-wise smooth equilibrium response $\hat{m}(\varepsilon)$.

We reiterate that using a similar re-formulation of the existing version of the MTM approach one can expect to be able to overcome the computationally challenging nonlinearity of a 'purely elastic' problem, whose numerical solution presents major computational difficulties in the fully tensorial multidimensional case. Note that in such a reformulation one can also expect to encounter the analogues of the familiar notions of a yield surface, represented by the ridges of the equilibrium-energy landscape, and of a flow rule, represented by a post-bifurcational response bringing the elastically destabilized system into the neighboring energy well. However, if in our zero-dimensional toy model those notions could be introduced by explicit conditions, similar notions in the multidimensional tensorial case can be expected to be much more obscure. Some glimpses of the emerging complexity can be seen already in a 2D scalar version of the MTM, where even if the elimination of the elastic fields and the explicit reduction to a discrete automaton prove possible, the 'diffused' analogues of the yield surface and the flow rule remain largely implicit (Salman and Truskinovsky, 2011, 2012).

3. Mesoscopic tensorial model (MTM)

In this section we finally outline the proposed CP-type version of the geometrically nonlinear tensorial MTM, which can serve as a generalization of the 'condensed' model of toy crystal plasticity presented in Section 2.

We follow the classical continuum CP, and replace the additive decomposition of the scalar strain into elastic and plastic contributions, adopted in Section 2, by the multiplicative decomposition $\mathbf{F} = \mathbf{F}_e\mathbf{F}_p$. However, instead of the continuous plastic distortion $\mathbf{F}_p$ of CP, we use its discrete (quantized) analogue. The function ψ, which depended in the toy model on a scalar variable, will be replaced by a rank-one convex function of the tensorial variable $\mathbf{F}_e$ (Carstensen et al., 2002). In view of the mesoscopic nature of the MTM, the parameter analogous to the meso-scopic length scale δ in the toy model will be kept small but finite. To make the presentation of the ensuing computationally efficient version of the MTM more transparent, we limit our attention to the simplest 2D Bravais crystals, those with square symmetry.

Matrix-valued spin variable. The central new step in the reformulation of the MTM is the introduction of the quantized plastic strain $\mathbf{F}_p$. From the discussion of the zero-dimensional model in Section 2 it is clear that the tensorial analogue of the scalar plastic strain m should be discrete, but now the implied quantization should reflect the structure of the lattice-invariant transformations of 2D Bravais lattices onto themselves (Wang et al., 1993; Waal, 1990; Kaxiras and Boyer, 1994).

As we have already mentioned, the global symmetry of such lattices is described by the infinite discrete group $\mathrm{GL}(2,\mathbb{Z})$ (Ericksen, 1980; Folkins, 1991; Parry, 1998; Engel, 2012; Michel, 2001). In fact, for the purpose of identifying plastic distortions, we can neglect reflections and limit our attention to the infinite discrete group $\mathrm{SL}(2,\mathbb{Z})$. The implied global symmetry entails a tensorial periodicity of the energy density and points to the existence of an infinite number of equivalent energy minima describing lattice-invariant shears (Baggio et al., 2019; Conti and Zanzotto, 2004; Pitteri and Zanzotto, 2002). It is also known that different domains of periodicity and the associated minima of the energy can be parametrized by a matrix $\mathbf{m}$ having integer-valued entries $m_{ij} \in \mathbb{Z}$ and $\det(\mathbf{m}) = 1$.

Given such a characterization of the matrix $\mathbf{m}$, we can now state a main assumption of the re-formulated MTM approach:

$$\mathbf{m} = \mathbf{F}_p^{-1}. \tag{3.16}$$

The idea of using $\mathbf{F}_p^{-1}$ as a measure of plastic distortion instead of the more conventional $\mathbf{F}_p$ (see, for instance, Clayton, 2010) apparently goes back to Noll (1967). The corresponding conceptual framework was further developed in Epstein and Maugin (1996), Davini (2001), Gupta et al. (2007); for recent reviews see Epstein and Elzanowski (2007) and Steigmann (2023). What makes our mesoscopic approach different from all this work, aimed at the macroscopic description of material inhomogeneity, is that we abandon the idea that $\mathbf{F}_p^{-1}$ is a continuous tensorial variable and restrict it to only discretized (quantized) values. The main role of the resulting 'spin'-type plastic distortion $\mathbf{F}_p$ is to select one 'energy well' among the infinitely many equivalent replicas inside the globally periodic energy landscape.

In view of the frame-indifference requirement, the globally periodic energy density $\psi(\mathbf{C})$ is defined in the configurational space of objective metric tensors $\mathbf{C} = \mathbf{F}^\top\mathbf{F}$. Due to the implied symmetry imposed by the action of the infinite discrete group, we must require that

$$\psi(\mathbf{C}) = \psi(\mathbf{m}^\top\mathbf{C}\mathbf{m})$$

for all $m \in \mathrm{SL}(2,\mathbb{Z})$. Such symmetry tessellates the configuration space into equivalent periodicity domains inside which the response can be considered as purely elastic. The discreteness of plastic strain is then simply a reflection of the discreteness of the tessellation of the configurational space.

We can then conclude that under the assumption (3.16), a relevant measure of plastic strain emerges as a matrix-valued spin variable. The necessity of using a discrete measure of plastic slip is a manifestation of the sub-continuum, meso-scopic nature of the MTM. Note that the coarse-graining of plastic strain, implied in the CP approach, invalidates this discreteness and therefore abandons the idea of resolving the associated meso-scopic phenomena.

In contrast, the main goal of the MTM is to capture at least some of the effects that become invisible in the continuum limit. Therefore, the MTM places considerable emphasis on the fact that plastic flow advances via a succession of 'strain quanta'. This idea is exemplified in the present re-formulation of the MTM, which introduces such configurational discreteness explicitly. It should be noted, however, that the implied quantization of the configurational space is scale-free, as it reflects only the periodicity of the atomic lattice, and not the existence of any internal length scale.

Yet, the observed structure of plastic fluctuations apparently points to the existence in crystal plasticity of an internal meso-scopic length scale. The introduction of an internal length scale also plays an important role of regularizing the otherwise ill-posed mathematical problem. Indeed, it has been long realized, see Ericksen (1973), that in view of the severe nonconvexity of the globally periodic configurational energy landscape, the energy minimization implicated in the case of quasi-static driving would necessarily lead in the continuum (scale-free) setting to a degenerate (fluid-like) mechanical response.

In view of all these observations and despite its continuum appearance, the MTM approach is designed to carry a finite internal scale. As we have already mentioned, this is achieved by complementing the configurational discreteness with spatial discreteness. The latter is brought in through the meso-scopic elements, inside which the deformation is considered to be affine. The refusal of the MTM to resolve inhomogeneities below a given cut-off length scale leads to the necessary loss of some microscopic information, conceivably without compromising the main meso-scopic phenomena of interest. For instance, even though the MTM sets some limits on the value of the achievable dislocation densities, this can be expected to only affect the breadth of the 'inertial range' (using the language of turbulence theory) in the probability distribution of the avalanches, but not the corresponding power-law exponent. Finally, we mention that, characteristically, neither configurational nor spatial discreteness is a part of the conventional macroscopic CP approach to crystal plasticity.

Fundamental elastic domain (FED). The first step in the proposed re-formulation of the MTM is to define the effective 'yield criterion'. In our setting this can be done by associating the discrete updates of the quantized plastic strain $\mathbf{m}$ with the crossing of the boundaries between the periodicity domains in the configurational space, each containing a single replica of the same elastic 'energy well' (Baggio et al., 2019).

The geometrically minimal domain of periodicity in the above sense is known as the 'fundamental domain' (FD) (Folkins, 1991; Parry, 1998; Engel, 2012; Michel, 2001). For our purposes it is more convenient to deal with the FD extended by including its independent images under the action of the finite point group of the lattice (Pitteri and Zanzotto, 2002). Such an extended fundamental domain is known as the Ericksen-Pitteri neighborhood (Conti and Zanzotto, 2004; Ericksen, 1989; Duistermaat and

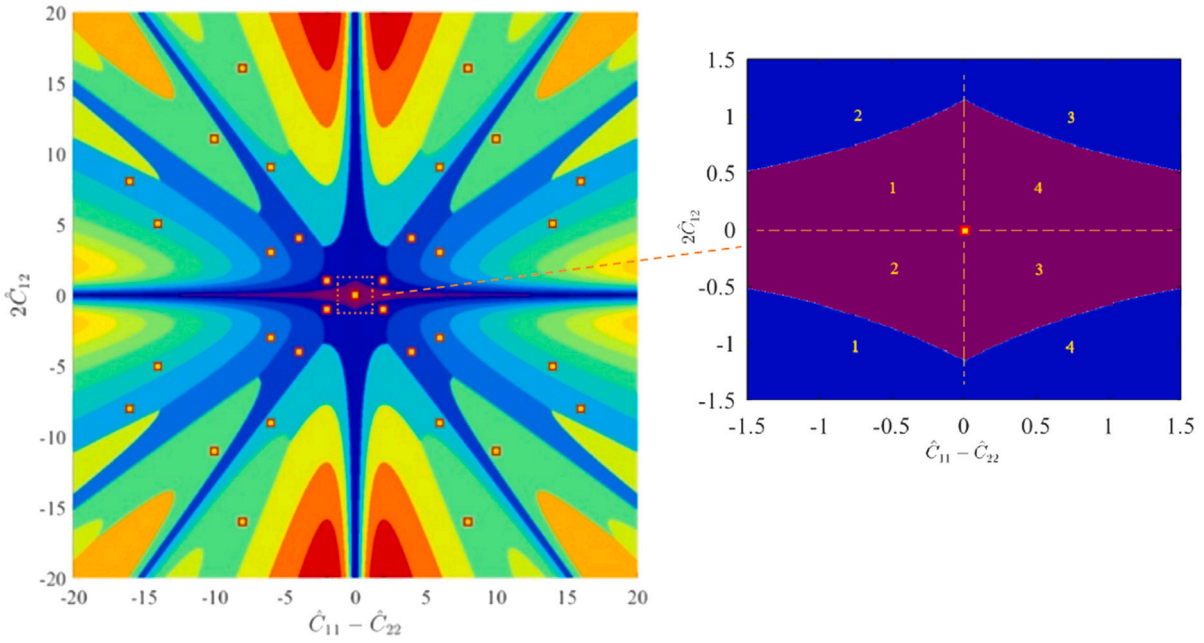

Fig. 7. The tessellation of the space of metric tensors $\hat{C}$ into equivalent elastic domains, each containing a single energy minimum. Thirty three minima of this type are identified by square markers. The inset on the right shows the FED (in magenta); for $\hat{C}_{12} \to 0$ the boundaries of the FED meet at $\hat{C}_{11} - \hat{C}_{22} = \pm\infty$. The numbers 1–4 correspond to four possible choices of FDs inside each choice of the FED.

Kolk, 1999; Pitteri, 1984b); in what follows we refer to it simply as the 'fundamental elastic domain' (FED). If configurational displacements are confined strictly to the interior of the FED (or to one of its equivalent images under the global symmetry transformation), then the deformation can be considered purely elastic. Instead, crossing the boundary of the FED implies the activation of plastic slip.

To locate this boundary we now turn to our special case of a simple square lattice defined by the basis vectors $\hat{\mathbf{e}}_1 = (1,0)^\top$ and $\hat{\mathbf{e}}_2 = (0,1)^\top$. Then the FED is characterized by the condition that in simple-shear loading its boundary is reached when an elementary-lattice cell reaches the kinematic mid-way towards the neighboring cell (Conti and Zanzotto, 2004). Therefore, outside such a domain the following inequalities are violated: $\hat{\mathbf{e}}_1^\top \mathbf{C}\hat{\mathbf{e}}_2 \le \frac{1}{2}\hat{\mathbf{e}}_1^\top \mathbf{C}\hat{\mathbf{e}}_1$, and $\hat{\mathbf{e}}_1^\top \mathbf{C}\hat{\mathbf{e}}_2 \le \frac{1}{2}\hat{\mathbf{e}}_2^\top \mathbf{C}\hat{\mathbf{e}}_2$ or, equivalently, $2|\hat{C}_{12}| \le \min(\hat{C}_{11}, \hat{C}_{22})$, where $\hat{\mathbf{C}} = \mathbf{C}/\det(\mathbf{C})$. Therefore, the interior of the FED in this case is defined by the conditions:

$$\left|\hat{C}_{11} - \hat{C}_{22}\right| \le \frac{1}{2}\left(\frac{1}{\left|\hat{C}_{12}\right|} - 3\left|\hat{C}_{12}\right|\right). \tag{3.17}$$

The ensuing global tessellation of the configurational space of metric tensors (symmetric 2D matrices with determinant equal to one) into equivalent elastic domains is illustrated in Fig. 7. Here different colors correspond to different but equivalent, symmetry-related, elastic domains, each containing a single energy-minimum. In the panel on the right we show a zoom on the FED. Note that it is divided, in turn, into four equivalent subdomains, each representing a replica of the geometrically minimal FD. Note also that in Fig. 7 we employed a particular parametrization of the configurational space using as coordinates two independent components of the metric tensor, namely, $\hat{C}_{12}$ and $\hat{C}_{11} - \hat{C}_{22}$. Various other possible parameterizations of the same space are discussed in Baggio et al. (2019), Salman et al. (2021), Baggio et al. (2023a).

The update rules. We have seen that under the condition of quasi-static driving the evolution of our quantized plasticity measure is expected to be a combination of two types of phenomena. First, there should be 'slow-time' stages, when plastic strain remains unchanged while elastic strain increases (quiescent periods). Second, there should be 'fast-time' stages, representing the transitions between different elastic-equilibrium branches (plastic events).

Observe that in the tensorial setting, plastic events necessarily imply the crossing of a boundary of one of the equivalent elastic domains. In the case of a 2D square lattice, such a boundary includes four sub-boundaries which correspond to the two slips (forward and backward) along the two main slip directions (vertical and horizontal). In Fig. 8 we present a schematic picture where we associate these four elementary transformations with the crossing of the corresponding sub-boundaries of the FED.

Suppose, next, that during a particular loading step, corresponding to, say, the kth plastic correction iteration, the local deformed configuration is described by the metric tensor $\hat{\mathbf{C}}_k$ and the measure of plastic strain is $\mathbf{m}_k$. Suppose also that the reduced metric tensor $\hat{\mathbf{C}}_k^e = \mathbf{m}_k^\top \hat{\mathbf{C}}_k \mathbf{m}_k$, which is the image of $\hat{\mathbf{C}}_k$ in the FED, is in compliance with the 'elastic stability' condition (3.17). Finally,

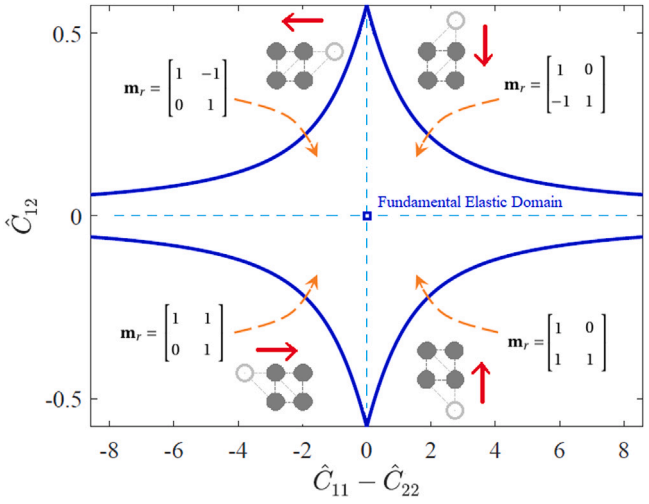

Fig. 8. A schematic figure linking different matrices $\mathbf{m}_r$ with different boundaries of the FED. The crystallographic structures illustrate the corresponding lattice-invariant shears.

assume that the associated displacement field does not ensure elastic equilibrium and an additional 'elastic' equilibration (elastic correction) step is required.

This step produces a new displacement field solving the elastic problem at fixed $\mathbf{m}_k$, which also generates a new local value of the metric tensor $\hat{\mathbf{C}}_{k+1}$. Using the known value of $\mathbf{m}_k$ we can compute the new value of the reduced metric tensor $\hat{\mathbf{C}}^e_{k+1}$ and check whether the 'yield condition' is respected, i.e. that the metric tensor $\hat{\mathbf{C}}^e_{k+1}$ is indeed inside the FED limits given by condition (3.17). If this condition is violated, the local deformed configuration described by the metric tensor $\hat{\mathbf{C}}^e_k$ lies outside the FED and one needs to activate a plastic correction by updating the plasticity measure from $\mathbf{m}_k$ to $\mathbf{m}_{k+1}$. The choice of the slip-plane to be activated and of the direction of the slip to be taken depends on the answer to the question which part of the boundary of the FED has been crossed. This choice ultimately controls the new value of the plastic strain measure $\mathbf{m}_{k+1}$.

The above abstract discussion can be re-stated in the form of an iterative algorithm. An elementary step of this algorithm can be written in the form:

$$\mathbf{m}_k \to \mathbf{m}_{k+1} = \mathbf{m}_k \mathbf{m}^r_k, \tag{3.18}$$

where

$$\mathbf{m}^r_k = \begin{cases} \begin{bmatrix} 1 & \mp 1 \\ 0 & 1 \end{bmatrix}, \ \pm 2\hat{C}^e_{k,12} > \hat{C}^e_{k,11} \text{ and } \hat{C}^e_{k,22} > \hat{C}^e_{k,11} \\ \begin{bmatrix} 1 & 0 \\ \mp 1 & 1 \end{bmatrix}, \ \pm 2\hat{C}^e_{k,12} > \hat{C}^{e,}_{k,22} \text{ and } \hat{C}^e_{k,11} > \hat{C}^e_{k,22}. \end{cases} \tag{3.19}$$

As an illustration of these general relations we now consider an example. Suppose that the update is performed using an elementary lattice-invariant shear of the form

$$\mathbf{m}^r_k = \begin{bmatrix} 1 & -1 \\ 0 & 1 \end{bmatrix}, \tag{3.20}$$

which corresponds to horizontal (clockwise) shear. Then $\hat{\mathbf{C}}^e_{k+1,11} = \hat{\mathbf{C}}^e_{k,11}$, $2\hat{\mathbf{C}}^e_{k+1,12} = -2\hat{\mathbf{C}}^e_{k,11} + 2\hat{\mathbf{C}}^e_{k,12}$ and the new reduced metric tensor is characterized by the following relations

$$\begin{aligned} 2\hat{\mathbf{C}}^e_{k,12} > \hat{\mathbf{C}}^e_{k,11} \Rightarrow 2\hat{\mathbf{C}}^e_{k+1,12} > -\hat{\mathbf{C}}^e_{k,11} = -\hat{\mathbf{C}}^e_{k+1,11} \ \Rightarrow 2\hat{\mathbf{C}}^e_{k+1,12} > -\hat{\mathbf{C}}^e_{k+1,11} \\ 2\hat{\mathbf{C}}^e_{k,12} < 3\hat{\mathbf{C}}^e_{k,11} \Rightarrow 2\hat{\mathbf{C}}^e_{k+1,12} < \hat{\mathbf{C}}^e_{k,11} = \hat{\mathbf{C}}^e_{k+1,11} \ \Rightarrow 2\hat{\mathbf{C}}^e_{k+1,12} < \hat{\mathbf{C}}^e_{k+1,11} \end{aligned} \tag{3.21}$$

In other words, if before the plastic correction we had $\hat{\mathbf{C}}^e_{k,11} < \hat{\mathbf{C}}^e_{k,22}, \hat{\mathbf{C}}^e_{k,11} < 2\hat{\mathbf{C}}^e_{k,12} < 3\hat{\mathbf{C}}^e_{k,11}$, and the conditions (3.17) were not satisfied, then after the plastic correction we have $|2\hat{\mathbf{C}}^e_{k+1,12}| < \hat{\mathbf{C}}^e_{k+1,11}$, which implies that the 'yield condition' is now satisfied. This indicates that the quantized plastic correction was performed adequately and that the discrete (quasi-)automaton has reached a stable fixed point. It is now straightforward to provide similar illustrations when 'plastic correction' implies the crossing of the other three smooth sub-boundaries of the FED (and involves the three other elementary matrices $\mathbf{m}^r_k$ in (3.19)).

The quasi-automaton epitomized in (3.18), (3.19) can be viewed as the analogue of the conventional incremental 'flow rule' postulated phenomenologically in classical CP. Two observations are in order. Note first that (3.18), (3.19) is not a real automaton

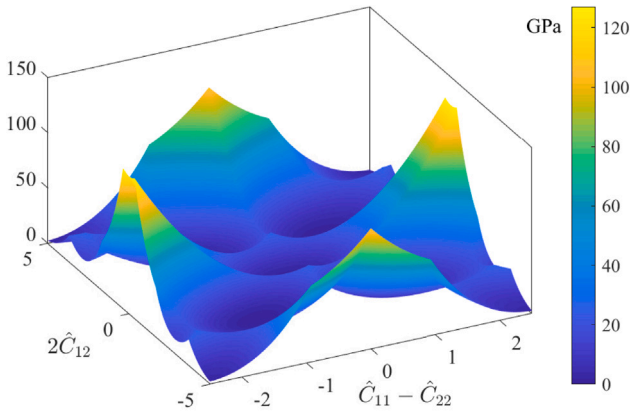

Fig. 9. Elastic energy density (3.22) for $J = 1$ extended periodically beyond the FED, with the parameter choice $\xi = 159.37$ GPa and $\eta = 160.72$ GPa, suitable for the description of ambient Tungsten (Featherstone and Neighbours, 1963).

formulated in terms of the 'condensed' variables only because the corresponding thresholds are not explicitly expressible in terms of the components of the integer-valued matrices $\mathbf{m}$. Such incomplete separability of the elastic and plastic problems is characteristic also for the continuum CP approach. Note next that in our particular setting the elementary 'plastic corrections' performed by the quasi-automaton involve two types of binary choices: of the slip system and of the slip direction. Both are governed exclusively by the structure of the energy landscape. Instead, in continuum CP such choices are not always unique (there are equivalent slip systems) and have to be made based on *ad hoc* phenomenological constitutive assumptions, see Forest (1998), Busso and Cailletaud (2005), Hartley and Kysar (2020), Dequiedt (2023).

Configurational energy landscape. As we have already explained, in the 'purely elastic' version of the MTM the discrete $\mathrm{SL}(2,\mathbb{Z})$ symmetry generates a natural tessellation of the configurational space of metric tensors into periodicity domains. In view of such (infinite) periodicity, the generic metric $\mathbf{C}$ with $\det(\mathbf{C}) = 1$ can be mapped onto the FED and the corresponding elastic response can always be described in terms of the reduced deformation measure $\mathbf{C}^e = \mathbf{m}^\top \mathbf{C}\mathbf{m}$. To construct the implied (infinitely) periodic configurational energy-density landscape in the space of *normalized* metric tensors

$$\hat{\mathbf{C}} = J^{-1}\mathbf{C},$$

where $J = \sqrt{\det(\mathbf{C})}$ describes the volumetric deformation, one needs to know the function ψ only inside the FED. Then it can be simply extended beyond this FED based on the periodicity.

With this idea in mind, we have chosen, for our numerical illustrations, to model the elastic response inside the FED by the simplest expression for the function $\psi(\mathbf{C}^e)$ respecting the point group symmetry of the square lattice and having several desirable properties as detailed below:

$$\psi(\mathbf{C}^e) = \frac{1}{2}\frac{K_{11}-K_{12}}{2}\left(\frac{C^e_{11}-C^e_{22}}{2}\right)^2 + \frac{1}{2}K_{44}(C^e_{12})^2 + \frac{1}{2}\frac{K_{11}+K_{12}}{2}(J-1)^2. \tag{3.22}$$

With J fixed, the elastic response is physically linear. The parameters K_{11}, K_{12}, K_{44} represent the standard cubic linear elastic moduli. In applications, one also encounters combinations of the same linear elastic constants, such as

$$\kappa = (K_{11}+K_{12})/2 > 0, \xi = (K_{11}-K_{12})/2 > 0, \eta = K_{44} > 0. \tag{3.23}$$

For instance, the dimensionless ratio

$$\mathcal{A} = \eta/\xi > 0 \tag{3.24}$$

is known in linear elasticity of cubic crystals as the Zener parameter (Walpole, 1986; Zener, 1948). While the simple formula (3.22) for the energy inside the FED was chosen to boost the numerical efficiency of the resulting algorithm, other expressions, having similar general properties, could be used as well, see Baggio et al. (2019, 2023b), where at least three other possible choices are discussed.

In Fig. 9 we illustrate the periodic continuation of the energy density (3.22) in the space of normalized metric tensors $\hat{\mathbf{C}}$, obtained through piece-wise smooth periodic extension from inside the FED to the entire configurational space. The material described by the energy density (3.22) is elastically 'well behaved' locally, as the associated equilibrium equations can be shown to satisfy the conditions of strong ellipticity inside the FED. Globally, the ensuing energy density is, of course, not rank-one convex, which is the reason we use it below only in a regularized setting.

Note that to emphasize the 'purely elastic' character of the resulting MTM and to ensure that the global energy is single-valued, the individual 'parabolic' branches of the energy density, shown in Fig. 9, were truncated outside each replica of the FED. However,

as we have explained in the discussion of the toy model, the new MTM framework, focusing on the evolution of the plastic strain measure $\mathbf{m}$, suggests that the individual 'parabolas' should not be truncated outside the limits of the corresponding FEDs.

The problem with such non-truncation would be that in the nonlinear setting the reliance on a multivalued energy density function may lead to artifacts. For instance, as we show below, additional constrains should be imposed on the coefficients in (3.22) to ensure that an elementary plastic correction in the resulting mutivalued-energy setting is always dissipative.

Dissipativity. Suppose that at a certain iteration involving plastic correction, the values of $\mathbf{m}$ and $\hat{\mathbf{C}}$ are such that $2\hat{C}^e_{12} > \hat{C}^e_{11}, \hat{C}^e_{11} < \hat{C}^e_{22}$ and therefore the conditions in (3.17) are violated; here $\hat{\mathbf{C}}^e = \mathbf{m}^\top \hat{\mathbf{C}}\mathbf{m}$ is the reduced (projected onto the FED) metric in a given iteration of the plastic correction. We suppose further that for small enough loading increments the metric $\hat{\mathbf{C}}^e$ violates the yield conditions only slightly.

A subsequent plastic correction produces the metric $\hat{\mathbf{C}}^{e\prime} = \mathbf{m}^{r\top}\hat{\mathbf{C}}^e\mathbf{m}^r$ with $\mathbf{m}^r$ given in (3.20) and therefore $\hat{C}^{e\prime}_{11} = \hat{C}^e_{11}, 2\hat{C}^{e\prime}_{12} = -2\hat{C}^e_{11} + 2\hat{C}^e_{12}$, $\hat{C}^{e\prime}_{22} = \hat{C}^e_{22} + \hat{C}^e_{11} - 2\hat{C}^e_{12}$. We can now introduce new variables (x, y) and (x', y') such that $0 < y' = 2\hat{C}^{e\prime}_{12} = 2\hat{C}'_{12} - 2\hat{C}^e_{11} < y = 2\hat{C}^e_{12}$ and $0 > x' = \hat{C}^{e\prime}_{11} - \hat{C}^{e\prime}_{22} = 2\hat{C}^e_{12} - \hat{C}^e_{22} > x = \hat{C}^e_{11} - \hat{C}^e_{22}$. Therefore, the plastic correction transforms the point (x, y) into the point (x', y') such that $x'^2 < x^2, y'^2 < y^2$. This plastic correction is dissipative if $\psi(x'^2, y'^2) < \psi(x^2, y^2)$ for all appropriate x, x', y, y'. Assuming that the energy density is smooth inside the FED, we can then write the conditions $\partial\psi(x^2, y^2)/\partial x^2 = C_1(x^2, y^2) > 0, \partial\psi(x^2, y^2)/\partial y^2 = C_2(x^2, y^2) > 0$, as sufficient for plastic dissipativity. In addition to the case $x < 0, y > 0$, considered above, we could also similarly consider the cases $x < 0, y < 0$, $x > 0, y < 0$ and $x > 0, y > 0$, and for all of them the obtained sufficient conditions guarantee dissipativity. For instance, the dissipativity is ensured if the energy density satisfies the conditions $C_1(x^2, y^2) = \text{const} > 0, C_2(x^2, y^2) = \text{const} > 0$. In the case of the energy density (3.22) these constraints reduce to inequalities to be satisfied by the elastic moduli, namely, $\xi = 8C_1 > 0, \eta = 8C_2 > 0$ and $\mathcal{A} = C_1/C_2 > 0$. In our numerical experiments we used the elastic parameters $K_{11} = 523.27$ GPa, $K_{12} = 204.53$ GPa, $K_{44} = 160.72$ GPa, corresponding to Tungsten at ambient conditions (Featherstone and Neighbours, 1963), which can be shown to be compatible with the plastic dissipativity constraints.

Numerical algorithm. In the absence of either PDE-based or ODE-based formulations, the discrete computational scheme, in itself, should be considered as a crucial element of the proposed mesoscopic approach to crystal plasticity.

The first step in designing such a scheme is to incorporate the globally periodic multivalued energy density into a spatially discretized framework. The discretization, representing physical regularization of the model, is obtained by introducing finite elements (FE) whose (coarse-grained, mesoscopic) mechanical response is assumed to be affine.

In our specific setting the FEM discretization is achieved by introducing a square grid of computational nodes, aligned with the presumed material crystallographic symmetry axes of the 2D crystal. Each square of the grid is then divided by the principal diagonal into two right isosceles triangular elements.

Note that the ensuing DE formulation contains an internal length scale h_0, the grid spacing, which is viewed as a physical parameter. The physical fields are then interpolated inside the elements using the most basic piecewise linear, tent-basis functions.

The *elastic* problem then reduces to finding the discrete displacement field $\mathbf{u}(\mathbf{x}) = \mathbf{y}(\mathbf{x}) - \mathbf{x}$ minimizing the total elastic energy of the system under the boundary conditions $\mathbf{u}|_{\mathbf{x}=\mathbf{x}_b} = \mathbf{u}_b(\alpha)$, where α is the loading parameter. The interpolated displacement field can be written in the form $\mathbf{u}(\mathbf{x}) = \sum_i \phi_i(\mathbf{x})\mathbf{U}_i$, where $\mathbf{x}$ are reference coordinates, $\phi_i(\mathbf{x}) = \int \mathbb{D}_{ij} d\mathbf{x}_j$ are the piecewise-linear, compact-support shape functions, and $\mathbb{D}_{ij}$ are matrices (of twelve variants) defined by

$$\begin{pmatrix} F_{11} \\ F_{12} \\ F_{21} \\ F_{22} \end{pmatrix} = \begin{pmatrix} 1 \\ 0 \\ 0 \\ 1 \end{pmatrix} + \mathbb{D} \begin{pmatrix} U^{(1)}_1 \\ U^{(2)}_1 \\ U^{(3)}_1 \\ U^{(1)}_2 \\ U^{(2)}_2 \\ U^{(3)}_2 \end{pmatrix}, \mathbb{D} = h_0^{-1} \begin{pmatrix} \mathbb{D}_0 & \mathbb{Z}_0 \\ \mathbb{Z}_0 & \mathbb{D}_0 \end{pmatrix}, \mathbb{Z}_0 = \begin{pmatrix} 0 & 0 \\ 0 & 0 \\ 0 & 0 \end{pmatrix}^\top, \mathbb{D}_0 = \pm \left(\mathbf{v}^{(i)}, \mathbf{v}^{(j\neq i)}, \mathbf{v}^{(k\neq i,j)} \right)_{i,j,k=1,2,3}; \mathbf{v}^{(1)} = \begin{pmatrix} 1 \\ 0 \end{pmatrix}, \mathbf{v}^{(2)} = \begin{pmatrix} 0 \\ 1 \end{pmatrix}, \mathbf{v}^{(3)} = \begin{pmatrix} -1 \\ -1 \end{pmatrix}.$$

Denoting the nodal displacements (column) vector by $\tilde{\mathbf{U}} = [\mathbf{U}_1^\top, \mathbf{U}_2^\top, \ldots]^\top$, we can write the total elastic free energy as a sum of the energies of the elements: $\bar{\Psi}(\tilde{\mathbf{U}}) = \sum_{i,j} V_i \psi\left(\mathbb{D}_{ij}\mathbf{U}_j, \mathbf{m}_i\right)$, where $V_i = h_0^2/2$ and $\mathbf{U}_i$ are nodal row vectors. In what follows the regularizing (cut-off) parameter h_0 is assumed to be fixed so that the question of mesh refinement is not posed; the optimal choice for the parameter h_0 will be discussed elsewhere. In all our numerical experiments we assumed that a linear displacement field compatible with (2.1) and parametrized by α is prescribed on the boundary of the domain (hard device). The boundary conditions are then $\mathbf{u}_b = [\mathbf{F}(\alpha) - \mathbf{I}]\mathbf{x}_b$.

In the description above we implicitly assumed that the original problem could be split into *elastic* and *plastic* problems. As we have seen the *elastic problem* pre-supposes that the set of integer-valued plastic strain variables $\mathbf{m}_i$ is known. Then, indeed the solution of the *elastic problem* consists in finding at each value of the loading parameter the energy-minimizing discrete set of displacement variables $\mathbf{U}_i$, for $i = 1, \ldots, n_x n_y$, representing the deformed locations of the nodes of the FE mesh. However, the set of plastic variables $\mathbf{m}_i$ should also emerge as an outcome of energy minimization modulo the condition that the entries in $\mathbf{m}_i$ always remain integer-valued with $\det(\mathbf{m}) = 1$, and that the plastic update only occurs if yield conditions applied to $\mathbf{U}_i, \mathbf{m}_i$ are violated. The challenge is to design an algorithm where the corresponding *plastic problem* is maximally separated from the elastic one.

In the proposed algorithm the parallel energy-minimization problems for $\mathbf{U}_i$ and $\mathbf{m}_i$ are solved at each increment of the loading in a sequence of two-step operations.

At the first, *predictor* stage, the response is assumed to be elastic and use is made of the tangent moduli calculated from the solution for the previous loading increment. The plastic strain $\mathbf{m}_i$ at this step is kept equal to the converged value from the previous increment of the loading.

At the second, *corrector* stage, we check in which elements the yield conditions were violated, perform plastic reduction there, and then solve the elastic problem again for the nodes associated with those elements in a fixed-boundary setting. Such refinement of the solution is performed iteratively, and at every iteration a new improved update for the plastic variables $\mathbf{m}_i$ is obtained, along with an improved update for the 'elastic variables' $\mathbf{U}_i$ (during each of such incremental refinements of the solution, plastic reduction is performed when needed, until the 'yield condition' (3.17) is satisfied everywhere).

More precisely, if in a given element the value of $\mathbf{C}_e$, calculated based on the current value of $\mathbf{m}$, falls outside the FED, the $\mathbf{m}$ matrix is updated. Then, (first-order) elastic energy minimization is performed by updating the global nodal displacements vector. Since the minimization is of the first order, a correction to the displacement field is chosen to be proportional to the vector of residual forces on the nodes (force mismatches at the nodes between adjacent elements). The corresponding pre-factor (step-size) is found by sub-iterations, to ensure the maximum energy decrease.

One noteworthy feature of the proposed approach is that the energy minimization procedure is implemented in a single loop over all the unstable elements and therefore there is no ambiguity regarding the order of the updates. Another one is that the coupling between the elements is only activated during the elastic predictor step – we discuss this in Appendix A, where the numerical implementation of the algorithm, involving a hybrid Gauss-Newton–Cauchy energy-minimization scheme, is presented in full detail.

Here we only mention that the additional numerical acceleration vis-a-vis the 'purely elastic' approach, achieved in the proposed algorithm, is due to the use of an elastic energy-density functional which is 'well-behaved' inside the FED. This allows the minimization algorithm to converge with only a small number of iterations, as the elastic problem is effectively solved 'on the fly'. Moreover, the piece-wise smooth structure of the configurational energy landscape allows one to avoid navigation through a complex configuration of saddle points. Instead, we use an efficient nonsmooth discrete mapping algorithm.

Further acceleration is achieved by the use of a Cauchy update during plastic corrections (which would otherwise take a significant portion of the computational effort in each increment) instead of the LBFGS update, as in the purely elastic approach. This allows one to recalculate at each iteration only those components of the energy gradient and only those contributions to the total energy that are associated with the elements that have just undergone plastic correction. In view of the achieved nearly complete separation between the continuous elastic and discrete plastic problems, we regard the proposed algorithm as a (quasi-)automaton. We discuss the computational efficiency of the developed numerical method in more quantitative terms in Appendix B.

Quenched disorder. In view of the massive degeneracy associated with the possibility of collective crossing of the 'ridges' of the energy landscape (the boundaries of the FED) in pristine crystals, some additional regularization is called-for. The problem is resolved in the proposed algorithm through the introduction of small quenched disorder.

To minimize the impact of such disorder, we randomized only the displacements on the boundary using the decomposition $\Delta\bar{\mathbf{U}}_b = \Delta\bar{\mathbf{U}}_b^{(o)} + \Delta\bar{\mathbf{U}}_b^{(d)}$, where the first term is the deterministic contribution

$$\Delta\bar{\mathbf{U}}_b^{(o)} = \Delta\mathbf{F}\mathbf{x}_b = \Delta\alpha \begin{bmatrix} 0 & 1 \\ 0 & 0 \end{bmatrix} \mathbf{x}_b, \tag{3.25}$$

while the second term, described by the relations

$${}^{(i)}\Delta\bar{\mathbf{U}}^{(d)}_{b_{\text{bot/top}}} \cdot \hat{\mathbf{e}}_1 = 0,\ {}^{(i)}\Delta\bar{\mathbf{U}}^{(d)}_{b_{\text{left/right}}} \cdot \hat{\mathbf{e}}_2 = 0,\ {}^{(i)}\Delta\bar{\mathbf{U}}^{(d)}_{b_{\text{left/right}}} \cdot \hat{\mathbf{e}}_1 = 0,{}^{(i)}\Delta\bar{\mathbf{U}}^{(d)}_{b_{\text{bot/top}}} \cdot \hat{\mathbf{e}}_2 = \delta_d^{(i)}, \tag{3.26}$$

depends on the random parameters $\delta_d^{(i)}$. The latter were sampled for each node i independently, using a Gaussian distribution with a zero mean and standard deviation $\mathfrak{s}$ which was chosen sufficiently small ($\mathfrak{s}/h_0 = 10^{-9}$) to exclude effects that could be interpreted as physically-significant, see Salman and Truskinovsky (2011), Zhang et al. (2020b).

To make our assumptions in (3.26) more transparent, we assume that a square crystal is deformed with four rigid plates (lines) of equal dimensions moving as a parallelogram (the bottom side being fixed). To mimick surface roughness along the sides of the sample, we assumed that the disorder affects only the components of the displacement field ${}^{(i)}\Delta\bar{\mathbf{U}}_b^{(d)}$ oriented along the normal to the boundaries. Also, for simplicity, the implied quenched disorder (3.26) was introduced only along the top and bottom (horizontal) boundaries (for it to be normal both to the surface and to the displacements). Since the corresponding two (top and bottom) loading plates were interpreted as having random 'bumps' on their surface, inducing compression, at the nodes at which the generated random displacements turned out to be tensile, the random components of ${}^{(i)}\Delta\bar{\mathbf{U}}_b^{(d)}$ were replaced by zeros.

Another factor that we attempted to take into account is the macroscopic nature of the quenched disorder. This consideration requires the characteristic length of the disorder to remain above the mesoscopic features of the model, characterized by the parameter h_0. In this respect, imposing random fluctuations on all boundary nodes would be in contradiction with the idea that the disorder is macroscopic. Therefore, the random corrections to the imposed boundary displacement field were neglected on some boundary nodes (by keeping only those values that were larger than the standard deviation).

Link to classical CP. To interpret the results of our meso-scopic numerical experiments in macroscopic terms, we need a quantitative basis for comparison of the MTM with CP. The first question is whether in the re-formulated MTM the increment of plastic strain, serving as the analogue of the plastic velocity gradient,

$$\mathbf{L}_p = \dot{\mathbf{F}}_p\mathbf{F}_p^{-1},$$

can be additively decomposed into rank-one components. In other words, the question is whether the proposed kinematic description is compatible with the CP ansatz

$$\mathbf{L}_p = \sum_{j=1}^{N_s} \dot{\gamma}_j \mathbf{s}^{(j)} \left[\mathbf{n}^{(j)}\right]^\top, \tag{3.27}$$

where the unit vectors $\mathbf{s}_j$ and $\mathbf{n}_j$ represent the tangent and normal vectors to crystallograpically-specific slip planes. Observe first that in the re-formulated MTM the analogue of the plastic velocity gradient is the quantized increment of plastic strain. Indeed, if we write

$$\mathbf{L}_p^{(k)} \Delta t = -\left(\mathbf{m}^{(k)}\right)^{-1} \Delta \mathbf{m}^{(k)},$$

where

$$\Delta \mathbf{m}^{(k)} = \mathbf{m}^{(k+1)} - \mathbf{m}^{(k)},$$

then using (3.19) we obtain $\mathbf{L}_p^{(k)} \Delta t = -\mathbf{m}_r^{(k)} + \mathbf{I}$. We can then express $\Delta \mathbf{m}_r^{(k)} \triangleq \mathbf{m}_r^{(k)} - \mathbf{I}$ as a sum of two rank-one tensors:

$$\Delta \mathbf{m}_r^{(k)} = -\mathbf{L}_p^{(k)} \Delta t = -\Delta \gamma_{12}^{(k)} \begin{bmatrix} 0 & 1 \\ 0 & 0 \end{bmatrix} - \Delta \gamma_{21}^{(k)} \begin{bmatrix} 0 & 0 \\ 1 & 0 \end{bmatrix}. \tag{3.28}$$

The next step is to combine the individual iterations constituting a plastic correction. Under the assumption that it is comprised of $k_* > 1$ fast time steps, we can write

$$\Delta \mathbf{m}_r^{(k_*)} = \prod_{k=1}^{k*} \mathbf{m}_r^{(k)} - \mathbf{I}.$$

Therefore in slow time

$$\mathbf{L}_p = \lim_{\Delta t \to 0} \left[-\frac{1}{\Delta t} \left[\prod_{k=1}^{k*} \mathbf{m}_r^{(k)} - \mathbf{I} \right] \right],$$

where $\Delta t = \sum_{k=0}^{k*} \Delta t_k$. Finally, in view of (3.28), we can write

$$\mathbf{L}_p = \dot{\gamma}_1 \begin{pmatrix} 1 \\ 0 \end{pmatrix} \begin{pmatrix} 0 & 1 \end{pmatrix} + \dot{\gamma}_2 \begin{pmatrix} 0 \\ 1 \end{pmatrix} \begin{pmatrix} 1 & 0 \end{pmatrix}, \tag{3.29}$$

where the pre-factors $\dot{\gamma}_j$ characterize the rates of the corresponding plastic slips. The ansatz (3.29) is in agreement with the classical CP representation of plastic slip rate (3.27) given that in 2D square lattices $s_i^{(j)} = \delta_{ji}$ and $n_i^{(j)} = 1 - \delta_{ji}$.

Coarse-grained response. Assume again that our computational domain, representing a sample, is a macroscopic square containing N mesoscopic square finite elements. This macroscopic square is deformed in simple shear to form a parallelogram and we can interpret the resulting total energy per volume of the sample as the coarse-grained elastic energy density associated with such shear deformation.

Since energy is material additive (and the elements are identical in Lagrangian volume) we can obtain the coarse-grained energy density simply by averaging the energy densities of the N finite elements:

$$\langle \psi \rangle = \frac{1}{N} \sum_i \psi_i. \tag{3.30}$$

Assuming elastic response and using definitions (3.22), (3.23) and (3.24), we can express the measure of the macroscopic geometric simple shear through the coarse-grained stored energy density (3.30), as follows:

$$\alpha_e = \sqrt{4\sqrt{\frac{1}{4}\mathcal{A}^2 + \frac{1}{2\xi}\langle \psi \rangle} - 2\mathcal{A}} \tag{3.31}$$

Note that expression (3.31) can be used to represent the elastic component of the macroscopic strain even outside the purely elastic regime. Next, applying the multiplicative elastoplastic decomposition to the entire computational domain, and substituting the assumption of simple horizontal shear, one obtains the macroscopic plasticity measure as

$$\langle -m_{12} \rangle = \alpha - \alpha_e \tag{3.32}$$

where α is the macroscopic applied shear strain measure.

We can also express the relevant component of the macroscopic shear stress as the derivative of the macroscopic energy with respect to the macroscopic strain

$$\langle P_{12} \rangle = \left. \frac{\partial \langle \psi \rangle}{\partial \alpha} \right|_{\alpha_e}. \tag{3.33}$$

Observe that this derivative should be calculated along an elastic branch, which means as the limit of a finite difference, with no plastic events in between.

Using such macroscopic measures we will obtain from our mesoscopic model the effective macroscopic constitutive relations, which can already allow comparison with experimental results.

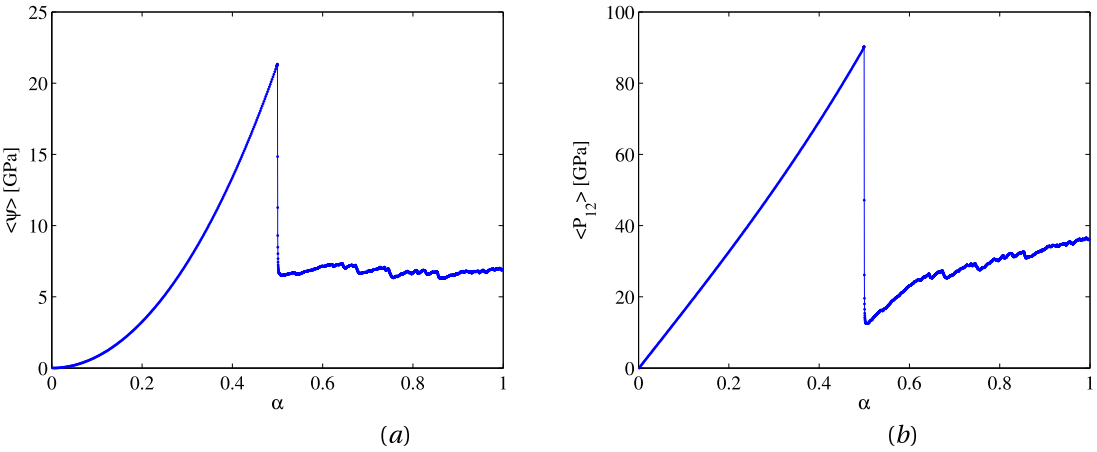

Fig. 10. Macroscopic constitutive response: (a) coarse-grained free-energy density versus applied macroscopic strain (scaling with the loading parameter α), (b) the coarse-grained shear stress versus α.

4. Case study

We now discuss the outcomes of our computational experiments, which were performed under several realizations of quenched disorder. Some of the results are presented after averaging over the disorder.

An initially-square domain was divided into $N = n \times n$ square cells with the linear side scale $h_0 = 1$ μm. The spatial resolution was set by the system size $n = 100$. The affine deformation (2.1) was applied incrementally to the nodes on the boundary of the computational domain (the four edges of the square computational box). The loading was updated with $\alpha_{l+1} = \alpha_l + \Delta\alpha$, starting from $\alpha_0 = 0$ (unloaded sample) up to $\alpha = 1$ (developed plasticity), with the value of the increment $\Delta\alpha = 2 \times 10^{-4}$ operative after the yield at $\alpha = 0.5$. Such a value of the increment was found to be sufficiently small to both fully resolve intermittent plastic avalanches and provide the convergence of the numerical algorithm.

Macroscopic constitutive response. In Fig. 10(a) we show the strain dependence of the coarse-grained energy density $\langle\psi\rangle$. The loading parameter α, introduced in (2.1) and (3.25), is changing quasistatically and at each value of this parameter a locally stable equilibrium state is reached as a result of energy minimization with respect to elastic and plastic degrees of freedom. For the same loading protocol we show in Fig. 10(b) the concurrent strain-induced evolution of the coarse-grained Piola–Kirchhoff stress tensor represented by the component $\langle P_{12}\rangle$, which is conjugate to the varying component of the applied distortion (3.25).

According to Fig. 10(a,b), in the interval $0 < \alpha < 0.5$ the response is elastic and the global deformation is (almost) affine, with all the elements following essentially identical trajectories in the configurational space of metric tensors (while remaining inside the FED). During this deformation stage, the fluctuations are effectively absent and the classical continuum elasticity theory is fully applicable. Despite the overall nonlinearity of the model, this purely elastic response along the simple shear deformation path is almost linear. The quenched disorder is apparently too small to cause any tangible plastic deformation. Such a stage is realistic only for specially grown pristine crystals and its main role here is to *prepare* a more generic state of the crystal with a meaningful configuration of crystal defects.

The role of such preparation is played by a system-size dislocations avalanche converting a singular (cold) configuration into a generic (hot) one. Such an avalanche takes place at $\alpha = 0.5$ when the configurational points collectively reach the boundary of the FED and the crystal undergoes massive instability. The system is frustrated due to the necessity to perform plastic correction simultaneously in almost all elements, and in our algorithm the associated massive correction is performed in a single loop over all the elements.

The system-size avalanche at $\alpha = 0.5$ proceeds (in fast time) through the nucleation of a large number of dislocations, which partially annihilate and partially self-organize inside the computational domain, eventually forming a complex post-avalanche spatial distribution of mutually locked dislocations. During this process the stress drops and a large amount of energy is dissipated. The dissipated energy is not accounted for directly, as we neglect the possibility of its transport by waves and keep the processes of thermalization and heat conduction unresolved.

As the loading process proceeds beyond $\alpha = 0.5$, we observe in Fig. 10(a,b) the emergence of pronounced fluctuations. Detailed analysis shows that intermittent dislocation avalanches intermix with extended periods of purely elastic behavior. Despite the overall macroscopic hardening, the elastic energy remains practically constant, as almost all the work of the loading device, accumulated during the elastic stages, is effectively dissipated during intermittent avalanches, see Fig. 10(a). The avalanches take the form of broadly distributed plastic events. The fact that after each of these events the energy is practically recovered during quiescent periods is in agreement with the general observation that the stored energy of cold work is extremely small.

As our re-formulation of the MTM gives us direct access to plastic strain, it is reasonable to raise the question of its dependence on the loading. A natural coarse-grained measure of plasticity attuned to our particular loading protocol is again $\langle -m_{12}\rangle$. As one

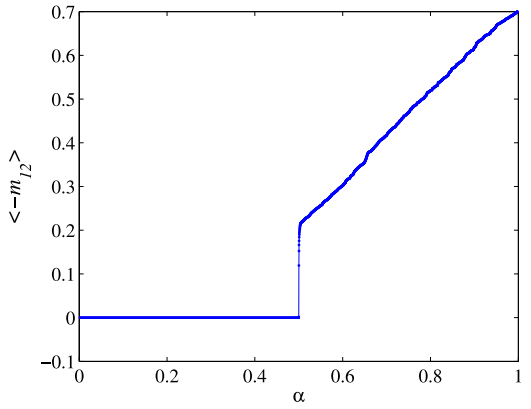

Fig. 11. Coarse-grained measure of plasticity (**m**) versus the loading parameter α.

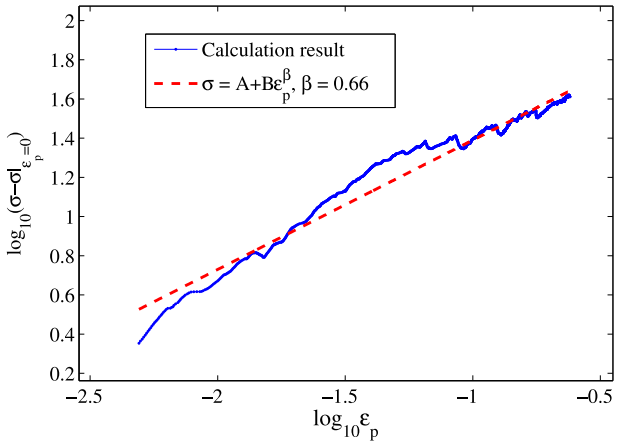

Fig. 12. Effective (von-Mises) stress vs. effective plastic strain (blue solid line with a dot marker) with a power-law fit for the trend (red dash), on a log–log scale – showing almost two decades of power-law behavior, the optimal fit producing the exponent $\beta = 0.66$.

can learn from Fig. 11, showing the dependence of this plastic strain measure on the loading parameter α, no plastic deformation takes place till the system reaches the boundary of the FED. After the system-size avalanche at $\alpha = 0.5$, plastic strain grows almost linearly with α. This power law correlation is another indication that the steady-hardening regime is (almost) scale free.

To characterize the after-yield ductile hardening regime more precisely, we show in Fig. 12 the relation between the averaged effective stress $\sigma \approx \sqrt{3}\langle P_{12}\rangle$ and the averaged effective small plastic strain $\epsilon_p = \frac{1}{2}\langle -m_{12}\rangle$. This relation is presented in log–log coordinates to show that it is in agreement with the well known phenomenological Johnson-Cook correlation, describing the dependence of the effective (von Mises) stress on plastic strain, $\sigma = A + B\epsilon_p^{\beta}$, the latter often being used to rationalize the results of physical experiments on polycrystalline-metal plasticity (Johnson and Cook, 1983). As we show below, the system-size avalanche practically turns the initial pristine single-crystal into an effective polycrystal, with no characteristic grain size, and the presence of such a power-law type correlation provides an evidence for the developing scale-free structure.

Interestingly, as our numerical experiments are targeting Tungsten-like 2D crystals, the obtained hardening exponent $\beta \approx 0.66$ (see Fig. 12) can be favorably compared to the exponent $\beta = 0.63$ obtained experimentally for polycrystalline Tungsten (Goh et al., 2017). We should note that the reason for our choosing of specifically Tungsten parameters is related to the fact that crystal Tungsten is one of the most elastically-isotropic elements, and therefore one can expect a 2D description be more representative of 3D behavior than for other elements, especially when comparison to 3D experiments is concerned. For less isotropic materials it is possible that complex 3D modes become the energetically favorable ones and they would be those that would underlie the mechanism responsible for observed response. Note also that correct coarse-grained plastic strain should be measured relatively to a value for which the microstructure is already randomized enough to represent real metals. We therefore define the plastic strain measure to be compared to the experimental one as plastic strain starting from the point where it beginds to grow approximately linearly with the applied global strain. For the performed calculations on the 2D crystal with Tungsten elastic constants, we get $\epsilon_p^* \approx 0.12$. Consequently, we set $\varepsilon_p = \epsilon_p - \epsilon_p^*$.

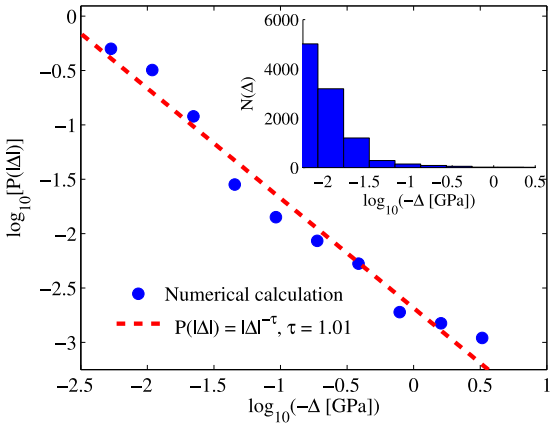

Fig. 13. Probability for energy-density drop Δ in a certain range of energy-density-drop magnitudes versus the middles of those ranges, on a log–log scale, with a linear-fit (red dashed line). The total number of avalanches in the power-law tail is 10,000 (obtained form 20 simulations), equal to the number of computational nodes, 10 boxes are used in the histogram, with a minimum of 10 avalanches in each box (the obtained exponent is locally insensitive to a change in the binning).

We terminated the loading protocol at $\alpha = 1.0$ under the assumption that the plastic flow, observed in the range $0.5 < \alpha < 1.0$, is steady, the system having reached a non-equilibrium steady state (NESS). This, however, may be a transient regime and new system-size avalanches may be expected as the loading extends beyond $\alpha = 1.0$. Such avalanches may be associated with the formation of shear bands, a major restructuring of dislocation cell structures and even the formation of cracks. These and other intriguing aspects of 'mature' plastic flows are left for future studies.

Temporal intermittency. As we have seen, in the regime of steady state plastic flow the system exhibits temporal fluctuations. We now discuss the statistical distribution of the corresponding plastic avalanches.

The nearly 1000 energy drops shown in Fig. 10 come in a broad range of magnitudes. In Fig. 13 we quantify these fluctuations by showing (using a log–log scale) the probability distribution of $\Delta\langle\psi\rangle$ to which we refer simply as Δ (the inset shows the actual histogram), based on a total of around 10,000 relatively large avalanches (from the high-energy tail of the distribution), obtained from 20 different runs, each with a different sample of quenched boundary disorder (with the same statistical parameters). The obtained distribution spans more than 2.5 decades; small and large scale cut-offs are not shown. A power law fit $P(\Delta) \sim \Delta^{-\tau}$ with the exponent $\tau = 1.01$ produces a good approximation. It is, again, suggestive of successful self-organization of the system towards scale-free NESS, reminiscent of developed turbulence (see Baggio et al., 2023b for additional arguments supporting this analogy). Note that the value of the power-law exponent, $\tau = 1$, is a signature of archetypically "wild" plasticity in the sense of Weiss et al. (2015).

It is also interesting that almost the same value of the power-law exponent ($\tau \approx 1$) was obtained in discrete dislocation dynamics (DDD) studies, which exhibited steady plastic flow in numerical experiments conducted on disorder-free 2D samples containing a fixed number of preexisting dislocations (Ispánovity et al., 2014; Salmenjoki et al., 2021). The exponent $\tau \approx 1$ was also recorded in numerical experiments involving pristine crystals conducted using the scalar version of the MTM (Zhang et al., 2020b). In the literature on crystal plasticity the exponent $\tau = 1$ is usually linked with either dislocation jamming or self-induced glassiness (Ovaska et al., 2015; Lehtinen et al., 2016; Zhang et al., 2016; Ruscher and Rottler, 2019). The reason is that this value of the exponent has previously emerged in a fully analytical mean-field theory of spin glasses, where it was associated with marginal stability (Pázmándi et al., 1999; Le Doussal et al., 2012; Franz and Spigler, 2017). Based on this analogy, we can argue that for low quenched disorder our system self-generates, through the first system-size avalanche, a 'mature' self-induced disorder, which appears to be bringing the system from a stable (elastic) to a marginally stable (glassy) state. The latter is known to emerge as a result of hierarchical (ultrametric) self-organization in the phase space (Müller and Wyart, 2015; Berthier et al., 2019). Using the same argument one can rationalize the fact that the exponent $\tau \approx 1$ has also been recorded in numerical studies of quasi-elastic flow regimes in structural glasses (Tyukodi et al., 2019; Ferrero and Jagla, 2019; Shang et al., 2020). More generally, the exponent $\tau = 1$ can be viewed as an indicator of the fact that in the course of self-organization the system has posited itself at the threshold of stability. Consequently, this value of the exponent can be seen as a marker of robust criticality, observable over a range of parameter values. Such criticality is different from the more conventional tuned criticality, occurring, for instance, when the system exhibits an isolated critical point in the parameter space (Christensen and Moloney, 2005; Sornette, 2006).

Spatial correlations. Our numerical experiments also allow one to visualize the emerging dislocation configurations and trace their development along the various stages of the overall deformation. In Fig. 14(a) we show the configuration of the computational nodes right after the occurrence of the first system-size avalanche taking place at $\alpha = 0.5$.

One can see again that as a result of the symmetry-breaking system-size plastic event, the affine state is destroyed through massive collective dislocations nucleation. Numerous concurrent slip events, developing in the fast time during this avalanche, transform a

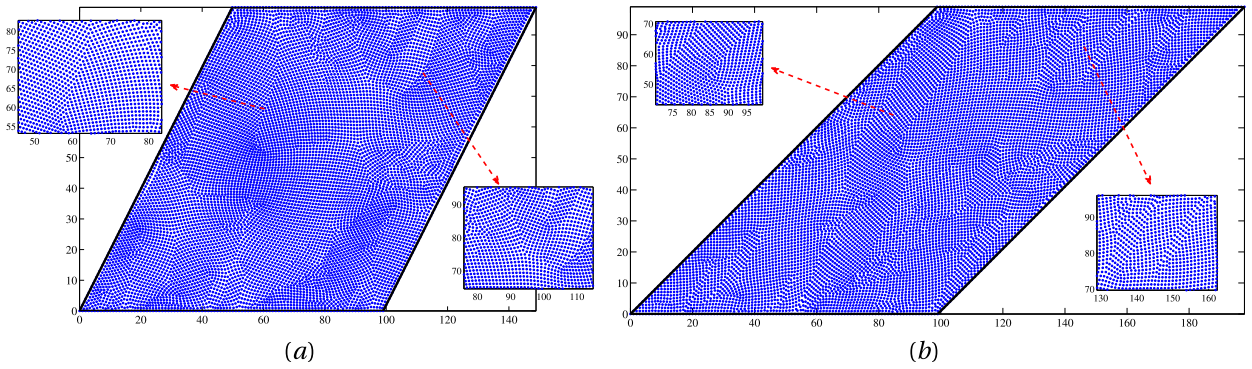

Fig. 14. (a) The positions of the nodes of the computational Lagrangian grid right after the first system-size avalanche, showing the emergence of a multigrain, polycrystal-type pattern; (b) the configuration of the nodes at the final state of deformation, showing the emergence of shear bands.

pristine crystal into a texture made of apparently randomly oriented grains. Each grain represents an almost unloaded (but rotated) version of the original square lattice and different grains are separated by dislocations-rich grain boundaries, which carry almost all the elastic energy (Baggio et al., 2023b). As an example, we can point to the two large grains in the top left quadrant of Fig. 14 (a), which are separated by an almost straight grain boundary (its crystallographic nature will be explored in detail in a separate paper). More complex patterns develop near the rough edges of the square domain, which serve as sources of strain concentration and contribute to heterogeneous nucleation of dislocations (Baggio et al., 2023a). The typical deformed configuration in the regime of developed plastic yield, $0.5 < \alpha < 1.0$, is shown in Fig. 14(b), which corresponds to $\alpha = 1$. It suggests that the post system-size avalanche grain structure evolves through smaller avalanches, increasing the complexity but not producing systematic configuration refinement. Some of the grains develop into elongated bands, inside which the lattice retains its nearly-square structure. The bands are separated from the rest of the lattice by dislocation-rich zones whose inner structure is finely tuned to the misorientation of the neighboring lattice patches. Overall, the size distribution of grain sizes remains broad and is characterized by long power-law tails (see below). The apparently scale-free plastic flow maintains its statistical signature despite the presence of stress-hardening and recurrent local restructuring.

Additional insight can be gained from the maps showing the distribution of the plastic strain measure $\mathbf{m}(\mathbf{x})$ at the final state where $\alpha = 1$, see Fig. 15. We observe that the dominant plasticity mode is horizontal simple shear aligned with the loading. However, such single-slip-system type plasticity affects only about three quarters of the elements, see Fig. 15(a). Due to self induced disorder, amplified by the system-size avalanche, the second main (simple shear) slip system is activated as well, see Fig. 15(b). Non-simple shear modes are activated too, but only within very few elements, see Fig. 15(c,d).

A meaningful measure of the observed spatial complexity emerges as we look at the occurrence of various types of plastic-slip events (increments of plastic deformation), focusing on the distribution of individual elements that have experienced a particular number of slips.

Our numerical experiments show that by the final stage of deformation (100% geometric shear strain), about 4500 out of almost 20,000 elements have experienced no plastic slip at all. This means that plasticity has spread over most of the sample and most of the elements have experienced at least one slip event. The analysis also shows that at the end ($\alpha = 1$) only a small number of elements has experienced two or more consecutive plastic-slip events.

These observations suggest that a relevant measure of the emerging spatial complexity (at this stage of the deformation) can be obtained if we focus on elements that have experienced no slip. This is illustrated in Fig. 16(a), where we show the spatial distribution of those 4500 elements, which exhibits a considerable degree of clusterization. The latter can be quantified if we evaluate the corresponding spatial correlation:

$$C(\zeta) \triangleq \frac{1}{N_0(N_0-1)} \sum_{j=1}^{N_0} \sum_{k \neq j}^{N_0} \mathcal{H}\left(\zeta - |\mathbf{x}_j - \mathbf{x}_k|\right), \tag{4.34}$$

where $\mathcal{H}(\cdot)$ is the Heaviside step function, $\mathbf{x}_i$ are the coordinates of the zero-slip elements and N_0 is the total number of elements in the computational domain which experienced no plastic slip. A log–log plot of the function in (4.34), revealing the emerging correlation, is presented in Fig. 16(b). The correlation dimension is computed from the slope inside the range where the correlation distance ζ is small enough for the chosen measure to be meaningful, but large enough with respect to the discretization resolution (around 3–6 finite-element side lengths). The computed value of the fractal dimension, $\nu = 1.65$, lies very close to the range [1.66,1.82] observed in the scalar model (Salman and Truskinovsky, 2011). It also falls inside the range [1.62,1.68] obtained in DDD analysis of FCC crystals (Hähner et al., 1998). The revealed evidence of scale-free spatial fluctuations is, again, indicative of complex hierarchical self-organization, at least in the intermediate range of scales, bounded on one side by the size of the system and on the other side by the cut-off scale.

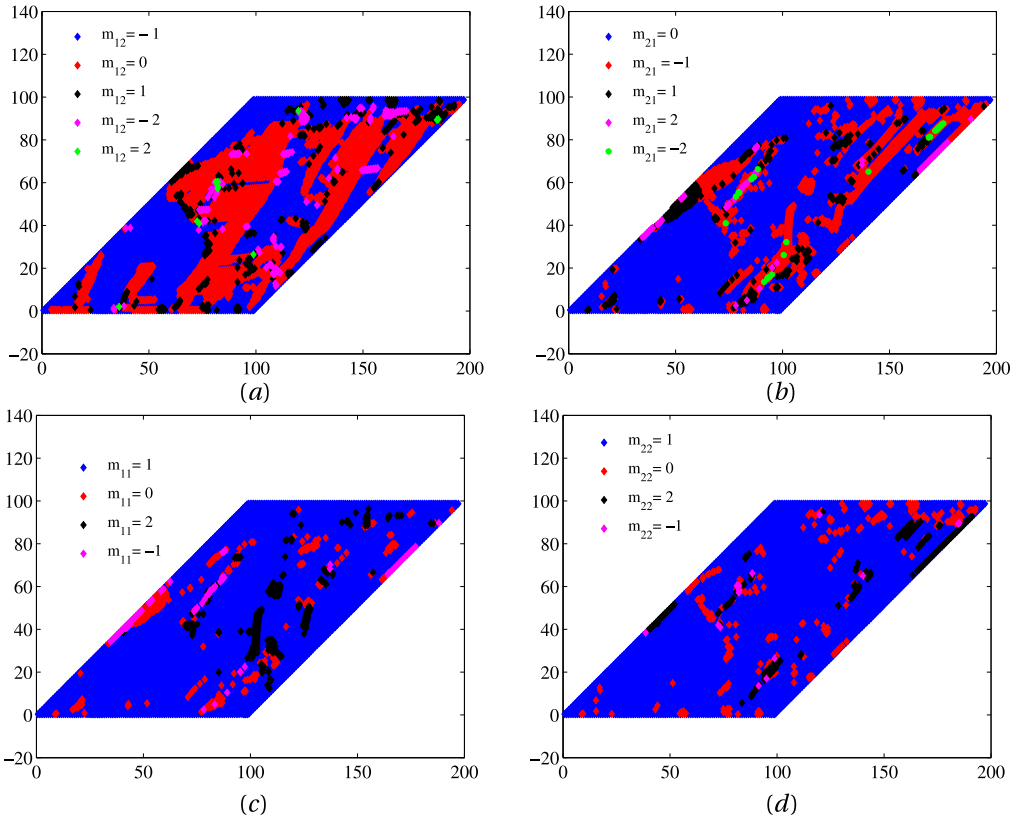

Fig. 15. Maps of the four different components of the plastic strain measure **m**, namely, (a) m_{12}, (b) m_{21}, (c) m_{11}, and (d) m_{22}.

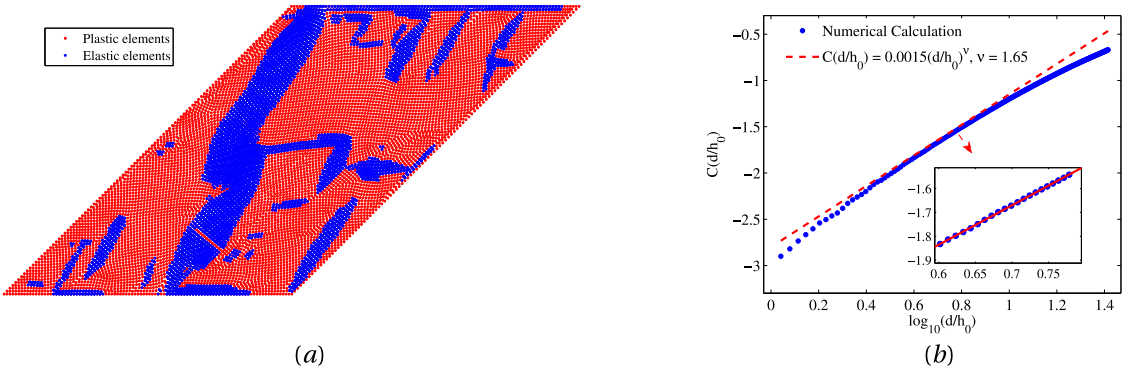

Fig. 16. (a) The centers of the elastic elements that had experienced no plastic slip during the deformation (blue dots) and the centers of elastic elements that have experienced at least one plastic slip (red dots) in the final state; (b) a log–log plot showing the correlation function (blue dots) along with a linear fit (red dash) revealing the value of the fractal dimension of the distribution of zero-slip elements, $\nu = 1.65$.

Different system size. To show that the main statistical characteristics of the plastic flow, identified in this study, are not affected by the system size, we present below some results of numerical experiments conducted for a smaller system, with 50 × 50 nodes, but with the same value of the internal length scale, h_0, see Fig. 17. We observe that while the statistical characteristics are expectedly less pronounced, the coarse-grained quantities and the fluctuation-statistics exponents computed for this smaller system agree fairly well with the ones obtained for the larger system with the 100 × 100 nodes. Indeed, in both cases the pre and post yield coarse-grained energy is around 20–25 GPa and 5–10 GPa, respectively, and the maximum post yield coarse-grained stress is around 30–40 GPa. Similarly, in both cases the initial post-yield and the final coarse-grained geometric plastic shear strain is around 0.2 and 0.7, respectively. The plastic-strain hardening exponent for both system sizes is in the range 0.63–0.66 and the avalanche sizes statistics is characterized by exactly the same tail exponent of 1.01. Similarly, the correlation dimension of the elastic zones pattern is size-independent, remaining in both cases at the value 1.65. It is indeed rather remarkable that all the aforementioned information can

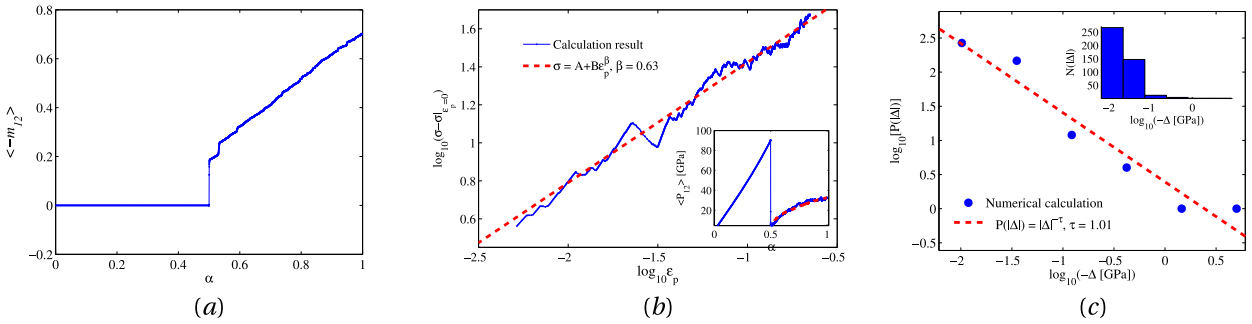

Fig. 17. Selected computational results for a smaller system, with $N = 50 \times 50$ nodes: (a) coarse-grained plasticity measure shear component versus applied macroscopic strain α, (b) macroscopic effective stress – small plastic strain relation on a log–log scale, showing almost two decades of power-law behavior with an exponent coinciding with the experimentally measured one. The inset shows the macroscopic stress–strain curve with the power-law approximation for the hardening part after the system-size avalanche; (c) Probability distribution of energy-density drops Δ on a log–log scale with a linear fit (red dashed line), showing the exponent of 1.01, exactly like in the $N = 100 \times 100$ case.

be obtained from a comparatively small system, with only 50×50 nodes, using an algorithm that runs for only half an hour on a standard *i*7 desktop computer. Needless to say that if instead of decreasing the system size we had increased it, the statistical quality of the results would have improved considerably, albeit at the price of considerable increase of the computational cost.

5. Conclusions

The paper offers a fundamental re-formulation of the MTM (mesoscopic tensorial model), which is a novel mesoscopic computational approach to crystal plasticity. The unique innovating nature of the MTM is in operating with the macro-scale notions of stress and strain while carrying some essential elements of the micro-scale physics of crystal lattices.

The MTM represents a crystal as an interacting collection of homogeneously deforming meso-scopic elastic elements whose nonlinear response is governed by a globally periodic elastic potential. The periodicity is designed to represent the full tensorial symmetry of Bravais lattices. On one side, the MTM can be viewed as a discretized continuum theory of the Landau type, with a tensorial strain as the order parameter and with lattice-invariant shears representing the minima of the equivalent energy wells. On the other side, it is expected to mimic the friction-type dissipation, which in conventional continuum theories of plasticity is associated phenomenolgically with active plastic mechanisms. Instead of being postulated, the implied dissipative structure emerges in the MTM naturally as an outcome of a homogenized description of a succession of instabilities experienced by an overdamped system on a rugged energy landscape.

Similarly to the Ginzburg–Landau theory, the MTM carries a regularizing parameter, which is, however, not associated with a gradient term in the energy, but rather arrives as a length scale representing the finite size of the mesoscopic elastic elements. This length scale describes the physical cut-off distance below which deformation is considered homogeneous (affine). It is viewed as a physically informed internal parameter and should not be confused with the mesh-size scale characterizing conventional discretization approximations.

An important aspect of the MTM is the precise account of geometric nonlinearity. The advantage of incorporating finite-strain kinematics into crystal plasticity theory is the possibility to adequately distinguish between different crystal-invariant shears while faithfully accounting for finite rotations. It is rather remarkable that those traditional aspects of nonlinear elasticity ended up being so crucial for plasticity theory.

A highly promising feature of the MTM as a fundamental and irreducible mesoscopic description of crystal plasticity, is that it is practically free of phenomenological assumptions. Even though it relies on the specifics of the interatomic potential, which is in principle sufficient for reconstructing the energy landscape, its global periodicity and the corresponding organization of the energy wells in the configurational space of metric tensors is universal, as it only depends on the symmetry of the crystal lattice. The precise nature of these equivalent wells and the value of the cut-off length scale appear to be irrelevant for the statistical structure of the resulting plastic flows. In this respect the MTM can be interpreted as the analogue of the Navier Stokes equations for crystal plasticity, carrying in the simplest form the essential nonlinearity, which turns out to be purely geometric.

The principal conceptual advance of the present paper in the context of the MTM framework is the *explicit* introduction of plastic strain. In its original formulation, the MTM is effectively a discretized nonlinear elasticity theory where plastic strain appears only *implicitly*. In the proposed re-formulation of the theory, plastic strain enters the model directly, in the form of a locally-defined integer-valued uni-modular matrix. A particular group-structure of the set of such matrices provides a geometrically-precise and crystalographically-specific description of lattice-invariant shears.

The main goal of the proposed re-formulation is to build a conceptual bridge between the MTM and the continuum CP theory. In the latter, the explicit distinction between elastic and plastic contributions to deformation allows one to effectively separate the conservative elastic prediction problem from the dissipative plastic correction problem. Moreover, in the CP, the conventional assumption that the elasticity is linear allows one to solve the elastic problem ‘on the fly’, while delegating all the complexity to a

separate nonlinear 'condensed' problem describing the evolution of the plastic strain. With the present paper, the same possibility becomes available inside the MTM framework. Furthermore, given the quantized nature of plastic deformation in the reformulated MTM, one can, in principle, relegate the evolution of plastic strain to a discrete automaton by minimizing out the elastic fields. In such an automaton, the driven overdamped dynamics in a rugged energy landscape would be effectively represented by a succession of discontinuous advances of quantized plastic strain. As we show, however, the complete separation of the elastic problem in the full geometrically nonlinear setting is problematic and, therefore, in the general case one can expect to formulate the reduced plastic problem at best as a quasi-automaton.

To reveal the inner mechanism of the re-formulated MTM, we opened the paper with a presentation of the fully analytical study of a zero-dimensional prototypical 'purely elastic' model of the depinning type. The mathematical transparency of such a model reveals why the evolution of the strain field in the MTM under quasi-static loading necessarily leads to a succession of quasi-elastic continuous stages interrupted by instantaneous quasi-plastic avalanches. It also explains how in the continuum limit, by accumulating infinitely many infinitely small avalanches of this type, one can obtain the characteristic rate-independent dissipation postulated in CP phenomenologically. We show that the analysis of this toy model naturally leads to the idea of separation between the elastic and plastic components of the deformation. Even more importantly, it provides the intuitive rationale for the ultimate configurational quantization of plastic strain. Needless to say that, in view of its oversimplified nature, the zero-dimensional model remains, at most, suggestive. In particular, it is unable to predict either the spatial or the temporal complexity of the observed plastic avalanches. It suggests then that a fully geometrically-faithful analogue should be developed and studied to capture the critical nature of plastic flows in crystals. The goal of the present paper was to show that the proposed re-formulation of the MTM is capable to serve this purpose.

The idea of solving, inside the MTM framework, the elastic and plastic problems separately was implemented in the new numerical algorithm detailed in the paper. An important technical challenge was to speedup the original, 'purely elastic', numerical algorithm, currently used in various applications of the MTM. From the computational perspective, the acceleration was achieved as a result of the transition from a soft-spin to a hard-spin formulation, which became possible when the description of the purely elastic part of the model was maximally simplified.

The main outcome of the proposed re-formulation of the MTM was an effective enslavement of continuous elastic deformation to the discrete evolution of the matrix-valued spin-field. While the proposed algorithm can indeed be viewed as producing a sequence of load-driven updates of such quantized plastic strain, as we have already mentioned, the geometric nonlinearity of the model implies that each of the updates necessarily contains an embedded implicit nonlinear energy-minimization step. In the adopted setting this step is practically straightforward due to the close to quadratic variation of the chosen elastic energy functional inside its periodicity domain.

Nevertheless, the solution still cannot be expressed in terms of an explicit 'elastic propagator' and therefore, as we have already explained, one can qualify the resulting discrete algorithm only as a quasi-automaton. In fact, we made it almost an automaton, since, with the chosen elastic energy function, a single Gauss-Newton minimization step (before plastic correction) is almost always sufficient for the convergence of the elastic problem. After a plastic correction a single (quickest-descent) Cauchy step is employed for the same purpose, which provides significant speedup, as a Cauchy step allows performing only local updates of the displacement field in each quasi-automaton iteration.

An important part of the paper is dedicated to the detailed analysis of the physical observations obtained in a set of numerical experiments. In these experiments, in which we studied the mechanical response of pure 2D crystals with square symmetry, subjected to simple shear, the main target was the emerging complexity resulting from the collective evolution of a large number of dislocations. The obtained results suggest that the proposed version of the MTM is capable of adequately reproducing the statistical structure of both temporal and spatial plastic fluctuations observed in several other independent numerical studies. This task is notoriously challenging due to the complex interplay in such a co-evolution of short and long range interactions among individual dislocations. The latter is what ultimately lies behind self-organization towards hierarchical structures and the associated intermittent dynamics.

Finally, we should mention that the use of the accelerated numerical approach was crucial for acquiring large-enough statistics to have convincing evidence that plastic fluctuations are indeed scale-free in a sufficient range of scales. The achieved computational speedup now paves the way towards using the MTM for the modeling of the distinctions between plastic fluctuations in 3D crystals with different crystallographic symmetries (e.g. HCP, FCC and BCC) and obtaining in this way the quantitative predictions that can lend themselves to direct comparison with physical experiments.

CRediT authorship contribution statement

N. Perchikov: Writing – review & editing, Writing – original draft, Validation, Software, Methodology, Investigation, Formal analysis, Data curation. **L. Truskinovsky:** Writing – review & editing, Writing – original draft, Supervision, Resources, Project administration, Investigation, Funding acquisition, Data curation, Conceptualization.

Declaration of competing interest

The authors declare that they have no known competing financial interests or personal relationships that could have appeared to influence the work reported in this paper.

Data availability

Data will be made available on request.

Acknowledgments

The authors are grateful to S. Conti and G. Zanzotto for helpful discussions at the initial stage of the project. Constructive practical suggestions by U. Salman given during the course of the project are deeply appreciated. We also thank S. Patinet for a careful reading of the manuscript. The authors appreciate the Agence National de la Recherche (ANR), France, grant No. 17-CE08-0047, for the financial support.

Appendix A. Numerical algorithm

As described in the main text, at each increment of the loading the energy-minimization problem for $\mathbf{U}_j$ at the nodes and $\mathbf{m}_i$ in the elements is solved in two steps.

At the first step, the elastic response is assumed to be linear, described by the tangent moduli calculated based on the solution at the previous loading increment; the set of plastic strains $\mathbf{m}_i$ at this step is kept equal to the stabilized value from the previous loading increment. The implied first-order Taylor-series expansion for the gradient of the energy in nodal displacements can be presented in the form:

$$d\bar{\Psi}/d\bar{\mathbf{U}}\big|_{\bar{\mathbf{U}}^*} = d\bar{\Psi}/d\bar{\mathbf{U}}\big|_{\bar{\mathbf{U}}_l} + \mathring{\mathbf{H}}^{(l)}(\bar{\mathbf{U}}^* - \bar{\mathbf{U}}_l),$$

where l denotes the previous loading increment for which a stable solution is known and

$$\mathring{\mathbf{H}}^{(l)} = \left.\frac{\partial^2\bar{\Psi}}{\partial\bar{\mathbf{U}}\partial\bar{\mathbf{U}}^\top}\right|_{\bar{\mathbf{U}}_l^\circ}.$$

The ensuing quadratic energy minimization problem reduces to the solution of a standard linear system of equations

$$\mathring{\mathbf{H}}^{(l)}(\Delta\bar{\mathbf{U}}^* - \Delta\bar{\mathbf{U}}_b) = \mathbf{b}_l,\ \mathbf{b}_l \triangleq -\mathbf{g}_l - \mathring{\mathbf{H}}^{(l)}\Delta\bar{\mathbf{U}}_b,\ \Delta\bar{\mathbf{U}}_* \triangleq \bar{\mathbf{U}}^* - \bar{\mathbf{U}}_l, \mathbf{g}_l \triangleq d\bar{\Psi}/d\bar{\mathbf{U}}\big|_{\bar{\mathbf{U}}_l}. \tag{A.1}$$

The crucial issue here is the location of the point at which the Hessian should be calculated.

Recall that for a function $\bar{\Psi}(\bar{\mathbf{U}})$ whose Hessian matrix is semi-positive-definite (SPD) everywhere, the solution of the linear system (A.1) always minimizes the energy. However, an objective energy density functional in principle cannot be convex everywhere as a function of the deformation gradient and thus the Hessian of the elastic energy would in general have some negative eigenvalues. In such cases, Newton's method with its first-order Taylor approximation would not necessarily bring the state closer to a solution of the equilibrium equations.

To remedy the problem we use a version of the Gauss-Newton approach (Gauss, 1809). In our case this means that instead of the local Hessian we would use the Hessian calculated at the bottom of the closest energy well, where some second derivatives vanish automatically. To be more specific, since under this choice one has $J = 1$ and $C^e_{11} - C^e_{22} = C^e_{12} = 0$, the non-SPD contributions to the Hessian are effectively eliminated. Moreover, since the Hessian is symmetric, the linear equations representing mechanical equilibrium can be solved by using the conjugate gradient (CG) method (Hestenes and Stiefel, 1952), with its optimal convergence characteristics.

Note, however, that in view of the objectivity-induced degeneracy of the bottom of the elastic energy well, one must specify how exactly the approximate Hessian should be calculated. Recall first that elastic distortion can be written in the form $\mathbf{F}_e = \mathbf{Fm}$. Using polar decomposition we can then write $\mathbf{Fm} = \mathbf{R}_e\mathbf{U}_e = \mathbf{R}_e\mathbf{C}_e^{1/2}$. The implied elastic rotation is thus $\mathbf{R}_e = \mathbf{FmC}_e^{-1/2}$. In our numerical algorithm we choose the Hessian to be calculated at the location (on the orbit representing the bottom of the energy well) corresponding to the current value of the plasticity measure $\mathbf{m}$ and the current value of the elastic rotation $\mathbf{R}_e$. In other words, the state at which the Gauss-Newton update is calculated, is chosen to be

$$\mathring{\mathbf{F}} = \mathbf{R}_e\mathbf{F}_p$$

which gives for the Hessian:

$$\mathring{\mathbf{H}} = \mathbf{H}|_{\mathbf{F}=\mathring{\mathbf{F}}},\ \mathring{\mathbf{F}} = \mathbf{FmC}_e^{-1/2}\mathbf{m}^{-1}. \tag{A.2}$$

The corresponding value of $\bar{\mathbf{U}}_l^\circ$ is then defined through

$$\mathring{\mathbf{F}}_{(i)} = \sum_j \mathbb{D}_{ij}\bar{\mathbf{U}}_l^{\circ,(j)},$$

where i denotes an element number and j denotes a node number. Similarly, the contributions of the nodes to the Hessian matrix is given by

$$\mathring{\mathbf{H}}^{(l)}_{(j,j')} = \sum_{i,i'} V_i\mathbb{D}^\top_{ij}\mathring{\mathbf{Q}}^{(i,i')}_l\mathbb{D}_{i'j'}.$$

While now Eq. (A.1) is well-posed at the internal nodes, at the boundary nodes the left-hand side may still vanish. This is corrected by using the augmented entries:

$$\bar{\mathbf{b}}_l \triangleq \begin{cases} \mathbf{b}_l, \mathbf{x} \in \Omega \\ 0, \mathbf{x} \in \partial\Omega, \end{cases} \qquad \bar{H}^{(l)}_{ij} \triangleq \begin{cases} \mathring{H}^{(l)}_{ij}, \mathbf{x} \in \Omega \\ 0, \mathbf{x} \in \partial\Omega, \ i \neq j \\ 1, \ \mathbf{x} \in \partial\Omega, \ i = j \end{cases} \tag{A.3}$$

where Ω and $\partial\Omega$ are the sets of internal and boundary nodes, respectively. Then the elastic predictor can be written in the form

$$\bar{\mathbf{U}}^* = \bar{\mathbf{U}}_l + \Delta\bar{\mathbf{U}}_b + \bar{\mathbf{H}}_l^{-1}\bar{\mathbf{b}}_l,$$

where the entries $\Delta\bar{\mathbf{U}}_b$ are presumed to be parametrized through α.

At the second step of the algorithm, plastic correction to the predicted displacement-field-increment is sought in a fixed-boundary setting. The predictor step should generally be large enough to drive some elements out of the elastic domain. The energy is minimized further by the operation of plastic reduction, during which $\mathbf{m}$ (and subsequently $\mathbf{g}^{(k)}_{l+1}$) is updated for elements not complying with (3.17). After this initial plastic reduction, the elastic problem is solved again for the nodes associated with the elements having just undergone active plastic reduction. The solution of this elastic problem consists in updating the displacement increment for the aforementioned nodes using a Cauchy maximum-descent step. Then, again, plastic reduction is performed for (some of) the elements associated with the nodes the displacement increment of which was just updated. After the yield conditions (3.17) have been satisfied for all the elements, final equilibrization is attained by a Gauss-Newton predictor step from the subsequent loading increment, which provides convergence for small-enough loading increments. The efficiency of the Gauss-Newton–Cauchy solver is due to the fact that the energy-density functional is close to a quadratic one, and any distinctly nonquadratic features (local nonconvexity) are circumvented by the calculation of the Hessian at the bottom of the energy well.

Note next that in the chosen piecewise smooth setting, during the plastic correction steps, the elements have to travel through 'ridges' of the energy landscape, occasionally reaching states where one cannot rely on tangent moduli. In such cases our numerical code activates a first-order Cauchy optimization algorithm (Cauchy, 1847). The corresponding gradient of the energy is pre-multiplied by a (positive) scalar (step-size), which is chosen to ensure the largest possible energy decrease. The corresponding algorithm can be written in the following form:

$$\bar{\mathbf{U}}^{(k=1)}_{l+1} = \bar{\mathbf{U}}^*, \ \bar{\mathbf{U}}^{(k+1)}_{l+1} = \begin{cases} \bar{\mathbf{U}}^{(k)}_{l+1} + \mathbf{d}^{(k)}_{l+1}, \mathbf{x} \in \Omega \\ \bar{\mathbf{U}}^{(k)}_{l+1}, \mathbf{x} \in \partial\Omega, \end{cases} \qquad \mathbf{d}^{(k)}_{l+1} = -\Delta t^{(k)}_{l+1}\mathbf{g}^{(k)}_{l+1}. \tag{A.4}$$

It should be noted that a positive step-size producing a decrease in the energy always exists. Indeed, for a small-enough positive value of the step-size, one can always use a second-order Taylor-series expansion to obtain

$$\begin{aligned} \hat{\Psi}^{(k+1)}_{l+1} \to \hat{\Psi}^{(k)}_{l+1} + \left[\mathbf{g}^{(k)}_{l+1}\right]^\top \left[\hat{\mathbf{U}}^{(k+1)}_{l+1} - \hat{\mathbf{U}}^{(k)}_{l+1}\right] + \frac{1}{2}\left[\hat{\mathbf{U}}^{(k+1)}_{l+1} - \hat{\mathbf{U}}^{(k)}_{l+1}\right]^\top \bar{\mathbf{H}}^{(k)}_{l+1}\left[\hat{\mathbf{U}}^{(k+1)}_{l+1} - \hat{\mathbf{U}}^{(k)}_{l+1}\right] = \\ = \hat{\Psi}^{(k)}_{l+1} - \Delta t^{(k)}_{l+1}\left|\mathbf{g}^{(k)}_{l+1}\right|^2 + \frac{1}{2}\left[\Delta t^{(k)}_{l+1}\right]^2\left[\mathbf{g}^{(k)}_{l+1}\right]^\top \bar{\mathbf{H}}^{(k)}_{l+1}\mathbf{g}^{(k)}_{l+1} < \hat{\Psi}^{(k)}_{l+1} \\ \forall \ \ 0 < \Delta t^{(k)}_{l+1} \ll \Delta t^{(k,l)}_{cr} = \frac{\left|\mathbf{g}^{(k)}_{l+1}\right|^2}{\frac{1}{2}\left|\left[\mathbf{g}^{(k)}_{l+1}\right]^\top \bar{\mathbf{H}}^{(k)}_{l+1}\mathbf{g}^{(k)}_{l+1}\right|} \end{aligned} \tag{A.5}$$

In order to determine the right step-size to employ in Eq. (A.4), an iterative process has to be used, with sub-iterations q. During those sub-iterations, the gradient $\mathbf{g}^{(k)}_{l+1}$ is kept fixed, and only the step size decreases, starting from a specified initial value. During the sub-iterations, the total elastic free energy ${}^{(q)}\hat{\Psi}^{(k+1)}_{l+1}$ is calculated until it becomes smaller than $\hat{\Psi}^{(k)}_{l+1}$. The step-size is then further varied until the minimum of ${}^{(q)}\hat{\Psi}^{(k+1)}_{l+1}$ is obtained with respect to q. As in the Armijo–Goldstein algorithm, exponentially decreasing linesearch over step-size is chosen, following the formula:

$${}^{(q)}\Delta t^{(k)}_{l+1} = \frac{\Delta t^{(k',l')}_{cr}}{2^q}, \quad q = \underset{q'}{\operatorname{argmin}}\, {}^{(q')}\hat{\Psi}^{(k+1)}_{l+1}, \ k' \in [1,k], \ l' \in [1,l] \tag{A.6}$$

where the choice of k', l' can generally be optimized for, with fewer sub-iterations for $k' = k, l' = l$ and fewer matrix multiplications for $k' = l' = 1$ (which was used in the case study in this work).

Our Fig. A.1 presents the detailed flow chart of the resulting algorithm (save for the details of the step-size determining procedure).

To summarize, in the proposed numerical approach for the corrector stage we first decrease the energy while tolerating possible exit from the 'elastic' domain for some elements. Only after the energy is minimized elastically and the maximal energy-decreasing step-size is found, the plastic step is performed, further reducing the energy. Then, another Cauchy step is attempted and if it does not drive any element out of the FED, the iterative procedure is considered terminated. The consecutive loading increment is then applied.

The described basic first-order optimization scheme can be considered efficiently accelerated in the following sense. The evaluation of the gradient vector is computer-time-consuming, as it requires a loop over all the elements, which adds linear complexity to the algorithm. A significant boost in computational efficiency (run-time) was obtained by avoiding performing a loop on all the elements. Thus, we are taking advantage of the fact that the plastic-corrector Cauchy-step can be activated only at

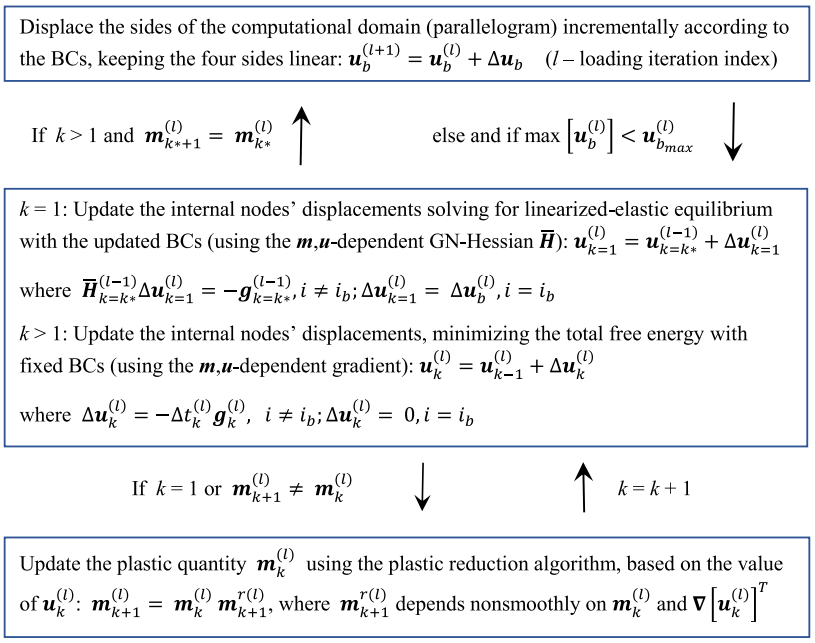

Fig. A.1. A flow chart of the solution algorithm (homogeneous initial conditions are assumed for the loading increment index $l \geq 1$; the convergent plastic iteration index k^* is defined implicitly through the convergence of $\mathbf{m}$ with k).

the nodes shared by elements in which $\mathbf{m}$ has changed in the previous iteration. Similar observations concern the computation of the total elastic energy which has to be recomputed for every sub-iteration for the determination of the step size. In the proposed accelerated approach the update for the energy in each iteration was computed by adding the increment in a loop only over the elements that have just undergone a plastic slip.

For the convenience of the readers and to make the underlying numerical machinery more explicit we finish this section by giving the expressions for the four components of the Piola–Kirchhoff stress tensor (calculated at a given $\mathbf{F}$) which were used to compute the residual nodal forces (from which the components of the gradient of the total energy – Cauchy directions – can be obtained as $\mathbf{g}_{(j)}^{(l)} = \sum_i V_i \mathbb{D}_{ij}^{\mathbb{T}} \mathbf{P}_l^{(i)}$):

$$\begin{aligned}
P_{11} &= \kappa F_{22}(F_{11}F_{22} - F_{12}F_{21} - 1) + \\
&+\frac{\xi}{4}\left[(m_{11}^2 - m_{12}^2)(F_{11}^2 + F_{21}^2) + 2(m_{11}m_{21} - m_{12}m_{22})(F_{11}F_{12} + F_{21}F_{22}) + \right. \\
&\left. +(m_{21}^2 - m_{22}^2)(F_{12}^2 + F_{22}^2)\right]\left[2F_{11}(m_{11}^2 - m_{12}^2) + 2F_{12}(m_{11}m_{21} - m_{12}m_{22})\right] + \\
&+\frac{\eta}{4}\left[2m_{11}m_{12}(F_{11}^2 + F_{21}^2) + 2(m_{12}m_{21} + m_{11}m_{22})(F_{11}F_{12} + F_{21}F_{22}) + \right. \\
&\left. +2m_{21}m_{22}(F_{12}^2 + F_{22}^2)\right]\left[4F_{11}m_{11}m_{12} + 2F_{12}(m_{12}m_{21} + m_{11}m_{22})\right]
\end{aligned} \tag{A.7}$$

$$\begin{aligned}
P_{12} &= -\kappa F_{21}(F_{11}F_{22} - F_{12}F_{21} - 1) + \\
&+\frac{\xi}{4}\left[(m_{11}^2 - m_{12}^2)(F_{11}^2 + F_{21}^2) + 2(m_{11}m_{21} - m_{12}m_{22})(F_{11}F_{12} + F_{21}F_{22}) + \right. \\
&\left. +(m_{21}^2 - m_{22}^2)(F_{12}^2 + F_{22}^2)\right]\left[2F_{12}(m_{21}^2 - m_{22}^2) + 2F_{11}(m_{11}m_{21} - m_{12}m_{22})\right] + \\
&+\frac{\eta}{4}\left[2m_{11}m_{12}(F_{11}^2 + F_{21}^2) + 2(m_{12}m_{21} + m_{11}m_{22})(F_{11}F_{12} + F_{21}F_{22}) + \right. \\
&\left. +2m_{21}m_{22}(F_{12}^2 + F_{22}^2)\right]\left[4F_{12}m_{21}m_{22} + 2F_{11}(m_{12}m_{21} + m_{11}m_{22})\right]
\end{aligned} \tag{A.8}$$

$$\begin{aligned}
P_{21} &= -\kappa F_{12}(F_{11}F_{22} - F_{12}F_{21} - 1) + \\
&+\frac{\xi}{4}\left[(m_{11}^2 - m_{12}^2)(F_{11}^2 + F_{21}^2) + 2(m_{11}m_{21} - m_{12}m_{22})(F_{11}F_{12} + F_{21}F_{22}) + \right. \\
&\left. +(m_{21}^2 - m_{22}^2)(F_{12}^2 + F_{22}^2)\right]\left[2F_{21}(m_{11}^2 - m_{12}^2) + 2F_{22}(m_{11}m_{21} - m_{12}m_{22})\right] + \\
&+\frac{\eta}{4}\left[2m_{11}m_{12}(F_{11}^2 + F_{21}^2) + 2(m_{12}m_{21} + m_{11}m_{22})(F_{11}F_{12} + F_{21}F_{22}) + \right. \\
&\left. +2m_{21}m_{22}(F_{12}^2 + F_{22}^2)\right]\left[4F_{21}m_{11}m_{12} + 2F_{22}(m_{12}m_{21} + m_{11}m_{22})\right]
\end{aligned} \tag{A.9}$$

$$\begin{aligned}P_{22} &= \kappa F_{11}(F_{11}F_{22} - F_{12}F_{21} - 1) + \\ &+\frac{\xi}{4}\left[(m_{11}^2 - m_{12}^2)(F_{11}^2 + F_{21}^2) + 2(m_{11}m_{21} - m_{12}m_{22})(F_{11}F_{12} + F_{21}F_{22}) + \right. \\ &\left. +(m_{21}^2 - m_{22}^2)(F_{12}^2 + F_{22}^2)\right]\left[2F_{22}(m_{21}^2 - m_{22}^2) + 2F_{21}(m_{11}m_{21} - m_{12}m_{22})\right] + \\ &+\frac{\eta}{4}\left[2m_{11}m_{12}(F_{11}^2 + F_{21}^2) + 2(m_{12}m_{21} + m_{11}m_{22})(F_{11}F_{12} + F_{21}F_{22}) + \right. \\ &\left. +2m_{21}m_{22}(F_{12}^2 + F_{22}^2)\right]\left[4F_{22}m_{21}m_{22} + 2F_{21}(m_{12}m_{21} + m_{11}m_{22})\right]\end{aligned} \tag{A.10}$$

We also present below explicit formulas for the ten second derivatives required for the calculation of the Gauss-Newton Hessian matrix evaluated at $\mathring{\mathbf{F}}$:

$$\begin{aligned}\mathring{Q}_{11} &= \kappa \mathring{F}_{22}^2 + \xi\left[\mathring{F}_{11}(m_{11}^2 - m_{12}^2) + \mathring{F}_{12}(m_{11}m_{21} - m_{12}m_{22})\right]^2 + \\ &+\frac{\xi}{2}(m_{11}^2 - m_{12}^2)\left[(m_{11}^2 - m_{12}^2)(\mathring{F}_{11}^2 + \mathring{F}_{21}^2) + 2(m_{11}m_{21} - m_{12}m_{22})(\mathring{F}_{11}\mathring{F}_{12} + \mathring{F}_{21}\mathring{F}_{22}) + \right. \\ &\left. +(m_{21}^2 - m_{22}^2)(\mathring{F}_{12}^2 + \mathring{F}_{22}^2)\right] + 2\eta m_{11}m_{12}\left[m_{11}m_{12}(\mathring{F}_{11}^2 + \mathring{F}_{21}^2) + (m_{12}m_{21} + m_{11}m_{22})(\mathring{F}_{11}\mathring{F}_{12} + \mathring{F}_{21}\mathring{F}_{22}) + \right. \\ &\left. +m_{21}m_{22}(\mathring{F}_{12}^2 + \mathring{F}_{22}^2)\right] + \eta\left[2\mathring{F}_{11}m_{11}m_{12} + \mathring{F}_{12}(m_{12}m_{21} + m_{11}m_{22})\right]^2\end{aligned} \tag{A.11}$$

$$\begin{aligned}\mathring{Q}_{12} &= -\kappa \mathring{F}_{21}\mathring{F}_{22} + \\ &+\xi\left[\mathring{F}_{11}(m_{11}m_{21} - m_{12}m_{22}) + \mathring{F}_{12}(m_{21}^2 - m_{22}^2)\right]\left[\mathring{F}_{11}(m_{11}^2 - m_{12}^2) + \mathring{F}_{12}(m_{11}m_{21} - m_{12}m_{22})\right] \\ &+\frac{\xi}{2}\left[(m_{11}^2 - m_{12}^2)(\mathring{F}_{11}^2 + \mathring{F}_{21}^2) + 2(m_{11}m_{21} - m_{12}m_{22})(\mathring{F}_{11}\mathring{F}_{12} + \mathring{F}_{21}\mathring{F}_{22}) + \right. \\ &\left. +(m_{21}^2 - m_{22}^2)(\mathring{F}_{12}^2 + \mathring{F}_{22}^2)\right](m_{11}m_{21} - m_{12}m_{22}) + \\ &+\eta\left[\mathring{F}_{11}(m_{12}m_{21} + m_{11}m_{22}) + 2\mathring{F}_{12}m_{21}m_{22}\right]\left[2\mathring{F}_{11}m_{11}m_{12} + \mathring{F}_{12}(m_{12}m_{21} + m_{11}m_{22})\right] + \\ &+\eta\left[m_{11}m_{12}(\mathring{F}_{11}^2 + \mathring{F}_{21}^2) + (m_{12}m_{21} + m_{11}m_{22})(\mathring{F}_{11}\mathring{F}_{12} + \mathring{F}_{21}\mathring{F}_{22}) + \right. \\ &\left. +m_{21}m_{22}(\mathring{F}_{12}^2 + \mathring{F}_{22}^2)\right](m_{12}m_{21} + m_{11}m_{22})\end{aligned} \tag{A.12}$$

$$\begin{aligned}\mathring{Q}_{13} &= -\kappa \mathring{F}_{12}\mathring{F}_{22} + \xi\left[\mathring{F}_{21}(m_{11}^2 - m_{12}^2) + \mathring{F}_{22}(m_{11}m_{21} - m_{12}m_{22})\right]\left[\mathring{F}_{11}(m_{11}^2 - m_{12}^2) + \mathring{F}_{12}(m_{11}m_{21} - m_{12}m_{22})\right] + \\ &+\eta\left[2\mathring{F}_{21}m_{11}m_{12} + \mathring{F}_{22}(m_{12}m_{21} + m_{11}m_{22})\right]\left[2\mathring{F}_{11}m_{11}m_{12} + \mathring{F}_{12}(m_{12}m_{21} + m_{11}m_{22})\right]\end{aligned} \tag{A.13}$$

$$\begin{aligned}\mathring{Q}_{14} &= \kappa(2\mathring{F}_{11}\mathring{F}_{22} - \mathring{F}_{12}\mathring{F}_{21} - 1) \\ &+\xi\left[\mathring{F}_{21}(m_{11}m_{21} - m_{12}m_{22}) + \mathring{F}_{22}(m_{21}^2 - m_{22}^2)\right]\left[\mathring{F}_{11}(m_{11}^2 - m_{12}^2) + \mathring{F}_{12}(m_{11}m_{21} - m_{12}m_{22})\right] \\ &+\eta\left[\mathring{F}_{21}(m_{12}m_{21} + m_{11}m_{22}) + 2\mathring{F}_{22}m_{21}m_{22}\right]\left[2\mathring{F}_{11}m_{11}m_{12} + \mathring{F}_{12}(m_{12}m_{21} + m_{11}m_{22})\right]\end{aligned} \tag{A.14}$$

$$\begin{aligned}\mathring{Q}_{22} &= \kappa \mathring{F}_{21}^2 + \xi\left[\mathring{F}_{12}(m_{21}^2 - m_{22}^2) + \mathring{F}_{11}(m_{11}m_{21} - m_{12}m_{22})\right]^2 + \\ &+\frac{\xi}{2}(m_{21}^2 - m_{22}^2)\left[(m_{11}^2 - m_{12}^2)(\mathring{F}_{11}^2 + \mathring{F}_{21}^2) + \right. \\ &\left. +2(m_{11}m_{21} - m_{12}m_{22})(\mathring{F}_{11}\mathring{F}_{12} + \mathring{F}_{21}\mathring{F}_{22}) + (m_{21}^2 - m_{22}^2)(\mathring{F}_{12}^2 + \mathring{F}_{22}^2)\right] + \\ &+\eta\left[2\mathring{F}_{12}m_{21}m_{22} + \mathring{F}_{11}(m_{12}m_{21} + m_{11}m_{22})\right]^2 + 2\eta m_{21}m_{22}\left[m_{11}m_{12}(\mathring{F}_{11}^2 + \mathring{F}_{21}^2) + \right. \\ &\left. +(m_{12}m_{21} + m_{11}m_{22})(\mathring{F}_{11}\mathring{F}_{12} + \mathring{F}_{21}\mathring{F}_{22}) + m_{21}m_{22}(\mathring{F}_{12}^2 + \mathring{F}_{22}^2)\right]\end{aligned} \tag{A.15}$$

$$\begin{aligned}\mathring{Q}_{23} &= -\kappa(\mathring{F}_{11}\mathring{F}_{22} - 2\mathring{F}_{12}\mathring{F}_{21} - 1) + \\ &+\xi\left[\mathring{F}_{21}(m_{11}^2 - m_{12}^2) + \mathring{F}_{22}(m_{11}m_{21} - m_{12}m_{22})\right]\left[\mathring{F}_{12}(m_{21}^2 - m_{22}^2) + \mathring{F}_{11}(m_{11}m_{21} - m_{12}m_{22})\right] \\ &+\eta\left[2\mathring{F}_{21}m_{11}m_{12} + \mathring{F}_{22}(m_{12}m_{21} + m_{11}m_{22})\right]\left[2\mathring{F}_{12}m_{21}m_{22} + \mathring{F}_{11}(m_{12}m_{21} + m_{11}m_{22})\right]\end{aligned} \tag{A.16}$$

$$\begin{aligned}\mathring{Q}_{24} &= -\kappa \mathring{F}_{11}\mathring{F}_{21} + \\ &+\xi\left[\mathring{F}_{21}(m_{11}m_{21} - m_{12}m_{22}) + \mathring{F}_{22}(m_{21}^2 - m_{22}^2)\right]\left[\mathring{F}_{12}(m_{21}^2 - m_{22}^2) + \mathring{F}_{11}(m_{11}m_{21} - m_{12}m_{22})\right] \\ &+\eta\left[\mathring{F}_{21}(m_{12}m_{21} + m_{11}m_{22}) + 2\mathring{F}_{22}m_{21}m_{22}\right]\left[2\mathring{F}_{12}m_{21}m_{22} + \mathring{F}_{11}(m_{12}m_{21} + m_{11}m_{22})\right]\end{aligned} \tag{A.17}$$

$$\begin{aligned}\mathring{Q}_{33} &= \kappa \mathring{F}_{12}^2 + \xi\left[\mathring{F}_{21}(m_{11}^2 - m_{12}^2) + \mathring{F}_{22}(m_{11}m_{21} - m_{12}m_{22})\right]^2 + \\ &+\frac{\xi}{2}(m_{11}^2 - m_{12}^2)\left[(m_{11}^2 - m_{12}^2)(\mathring{F}_{11}^2 + \mathring{F}_{21}^2) + 2(m_{11}m_{21} - m_{12}m_{22})(\mathring{F}_{11}\mathring{F}_{12} + \mathring{F}_{21}\mathring{F}_{22}) + \right. \\ &\left. +(m_{21}^2 - m_{22}^2)(\mathring{F}_{12}^2 + \mathring{F}_{22}^2)\right] + \eta\left[2m_{11}m_{12}\mathring{F}_{21} + \mathring{F}_{22}(m_{12}m_{21} + m_{11}m_{22})\right]^2 + \\ &+2\eta m_{11}m_{12}\left[m_{11}m_{12}(\mathring{F}_{11}^2 + \mathring{F}_{21}^2) + (m_{12}m_{21} + m_{11}m_{22})(\mathring{F}_{11}\mathring{F}_{12} + \mathring{F}_{21}\mathring{F}_{22}) + m_{21}m_{22}(\mathring{F}_{12}^2 + \mathring{F}_{22}^2)\right]\end{aligned} \tag{A.18}$$

$$\begin{aligned}\mathring{Q}_{34} = -\kappa\mathring{F}_{11}\mathring{F}_{12}+\\ +\xi\left[\mathring{F}_{21}(m_{11}m_{21}-m_{12}m_{22})+\mathring{F}_{22}(m_{21}^2-m_{22}^2)\right]\left[\mathring{F}_{21}(m_{11}^2-m_{12}^2)+\mathring{F}_{22}(m_{11}m_{21}-m_{12}m_{22})\right]+\\ +\frac{\xi}{2}(m_{11}m_{21}-m_{12}m_{22})\left[(m_{11}^2-m_{12}^2)(\mathring{F}_{11}^2+\mathring{F}_{21}^2)+2(m_{11}m_{21}-m_{12}m_{22})(\mathring{F}_{11}\mathring{F}_{12}+\mathring{F}_{21}\mathring{F}_{22})+\right.\\ \left.+(m_{21}^2-m_{22}^2)(\mathring{F}_{12}^2+\mathring{F}_{22}^2)\right]+\\ +\eta\left[\mathring{F}_{21}(m_{12}m_{21}+m_{11}m_{22})+2\mathring{F}_{22}m_{21}m_{22}\right]\left[2\mathring{F}_{21}m_{11}m_{12}+\mathring{F}_{22}(m_{12}m_{21}+m_{11}m_{22})\right]+\\ +\eta(m_{12}m_{21}+m_{11}m_{22})\left[m_{11}m_{12}(\mathring{F}_{11}^2+\mathring{F}_{21}^2)+(m_{12}m_{21}+m_{11}m_{22})(\mathring{F}_{11}\mathring{F}_{12}+\mathring{F}_{21}\mathring{F}_{22})+\right.\\ \left.+m_{21}m_{22}(\mathring{F}_{12}^2+\mathring{F}_{22}^2)\right]\end{aligned} \tag{A.19}$$

$$\begin{aligned}\mathring{Q}_{44} = \kappa\mathring{F}_{11}^2+\xi\left[\mathring{F}_{22}(m_{21}^2-m_{22}^2)+\mathring{F}_{21}(m_{11}m_{21}-m_{12}m_{22})\right]^2+\\ +\frac{\xi}{2}(m_{21}^2-m_{22}^2)\left[(m_{11}^2-m_{12}^2)(\mathring{F}_{11}^2+\mathring{F}_{21}^2)+2(m_{11}m_{21}-m_{12}m_{22})(\mathring{F}_{11}\mathring{F}_{12}+\mathring{F}_{21}\mathring{F}_{22})+\right.\\ \left.+(m_{21}^2-m_{22}^2)(\mathring{F}_{12}^2+\mathring{F}_{22}^2)\right]+\eta\left[2\mathring{F}_{22}m_{21}m_{22}+\mathring{F}_{21}(m_{12}m_{21}+m_{11}m_{22})\right]^2+\\ +2\eta m_{21}m_{22}\left[m_{11}m_{12}(\mathring{F}_{11}^2+\mathring{F}_{21}^2)+(m_{12}m_{21}+m_{11}m_{22})(\mathring{F}_{11}\mathring{F}_{12}+\mathring{F}_{21}\mathring{F}_{22})+m_{21}m_{22}(\mathring{F}_{12}^2+\mathring{F}_{22}^2)\right].\end{aligned} \tag{A.20}$$

Appendix B. Algorithmic efficiency

We begin with the general observation that, independently of the FE regularization, the main conceptual advantage of introducing the notion of plastic strain is the possibility to split a single incremental minimization problem of finding the deformation field $\mathbf{y}(\mathbf{x})$, in a setting where the associated globally periodic energy density *is not rank-one convex*, into two problems: one, of finding an integer-valued field $\mathbf{m}(\mathbf{x})$ with $\det(\mathbf{m}) = 1$, and another one, of finding the continuous field $\mathbf{y}(\mathbf{x})$ whose metric tensor $\mathbf{C}^e(\mathbf{x})$ (calculated based on $\mathbf{m}(\mathbf{x})$) is confined to the FED, where the energy *is rank-one convex*.

While the FE regularization makes the problem well posed, the geometric nonlinearity, which cannot be neglected due to the ubiquitous presence of large rotations in elastoplastic flows (Baggio et al., 2023a,b), makes the numerical implementation of the whole algorithm nontrivial. More specifically, while one can schematically describe this algorithm as a sequence of load-driven updates of the plastic variables $\mathbf{m}$, the apparent discrete-automaton type structure comes with a caveat that each update of $\mathbf{m}$ contains an embedded elastic energy-minimization step. Behind this incomplete separability of the elastic and plastic problems is the unavoidable geometrical complexity of the tensorial elastic problem, whose solution cannot be expressed in terms of an explicit 'elastic propagator' as in the simpler scalar version of the MTM (Salman and Truskinovsky, 2011, 2012; Zhang et al., 2020a).

Still, since in the proposed setting the solution of the elastic problem is manageable, due to the close to quadratic behavior of the elastic energy inside the FED, one can favorably compare the algorithmic complexity of the proposed algorithm with that of the 'purely elastic' algorithm used in Baggio et al. (2019, 2023a), Salman et al. (2021), Baggio et al. (2023b).

First, we note that in the 'purely elastic' approach one has to rely on the computationally-expensive quasi-Newton solver, as the task is always to minimize a highly non-convex function, which implies a large number of computational steps for each increment of the loading parameter. To make an estimate of the computational cost associated with such an algorithm, we can assume that the loading increment is $\Delta\alpha = 10^{-6}$–10^{-5} as in Baggio et al. (2019, 2023a), Salman et al. (2021), Baggio et al. (2023b). Given that the adopted quasi-Newton algorithm would have to deal with tens of thousands of variables, no less than $n_s = 100$ solver steps would be usually needed (Perchikov and Aboudi, 2020). Since in each of these steps the gradient of the energy has to be calculated using a loop over all the elements, we obtain an estimate of around $10^7 aN$–$10^8 aN$ operations, where a is the number of basic operations needed to compute a single entry of the gradient and N is the number of entries. The energy gradient has to be multiplied by the quasi-Newton matrix, which requires an update of the entire energy gradient with pN operations where $p \sim n_s$. For $N = 100 \times 100 = 10^4$ this gives around $10^{13}a$–$10^{14}a$ operations along the loading path stretching up to 100% geometric shear.

Instead, using the proposed framework, we found empirically for the same type of problem that the choice of the loading increment of $\Delta\alpha = 2 \times 10^{-4}$ was sufficient. In each increment, at least for $N = 100 \times 100$, the required total number of operations was around 1.5 times the number of operations in the corresponding linear elasticity problem (a single Gauss-Newton step for each increment) because the computational cost of plastic correction was approximately half of that of the elastic prediction. Note also that due to the chosen exponential variation of the time-step with the sub-iterations (say, when using line-search as in Armijo (1966)), the additional computational time associated with such sub-iterations is only logarithmic in the required number of sub-iterations, and can be kept bounded. Therefore, the overall gain in run-time due to the proposed accelerating measures is significant, and reaches at least an order of magnitude, vis-a-vis the formal looping over all elements.

Overall, we observed (for the $N = 100 \times 100$ case) that the iterations associated with plastic corrections converged, on average, in about 30 function calls (automaton iterations plus step-size determining sub-iterations), with around 30 elements updated in each automaton step. This amounts to around $10^3 b$ operations for the plastic corrector stage, where $b \sim a$ is a constant characterizing the effort of the computation of the Jacobian and $a \approx 7$, which translates to only about 20 microseconds on a simple 4-core *i*7 desktop computer. An even more detailed counting, which will be presented elsewhere, suggests that the proposed reformulation of the MTM framework can lead to an up to two orders of magnitude decrease in the computational time vis-a-vis the more conventional, 'purely elastic', MTM approach.

References

Abeyaratne, R., Chu, C., James, R.D., 1996. Kinetics of materials with wiggly energies: theory and applications to the evolution of twinning microstructures in a Cu-Al-Ni shape memory alloy. Phil. Mag. A 73 (2), 457–497.

Armijo, L., 1966. Minimization of functions having Lipschitz continuous first partial derivatives. Pacific J. Math. 16 (1), 1–3.

Arminjon, M., Imbault, D., 2021. Does a polycrystal model disclose a single plastic spin? In: Large Plastic Deformations: Fundamental Aspects and Applications To Metal Forming. Routledge, pp. 89–100.

Asaro, R.J., 1983. Crystal Plasticity. pp. 921–934.

Baggio, R., Arbib, E., Biscari, P., Conti, S., Truskinovsky, L., Zanzotto, G., Salman, O.U., 2019. Landau-type theory of planar crystal plasticity. Phys. Rev. Lett. 123, 205501.

Baggio, R., Salman, O.U., Truskinovsky, L., 2023a. Homogeneous nucleation of dislocations as a pattern formation phenomenon. Eur. J. Mech. A Solids 99, 104897.

Baggio, R., Salman, O.U., Truskinovsky, L., 2023b. Inelastic rotations and pseudoturbulent plastic avalanches in crystals. Phys. Rev. E 107 (2), 025004.

Berthier, L., Biroli, G., Charbonneau, P., Corwin, E.I., Franz, S., Zamponi, F., 2019. Gardner physics in amorphous solids and beyond. J. Chem. Phys. 151, 010901.

Boyce, M.C., Weber, G.G., Parks, D.M., 1989. On the kinematics of finite strain plasticity. J. Mech. Phys. Solids 37 (5), 647–665.

Boyer, L.L., 1989. Magic strains in face-centered and body-centered cubic lattices. Acta Crystallogr. Sect. A 45.9, fc29–fc32.

Busso, E.P., Cailletaud, G., 2005. On the selection of active slip systems in crystal plasticity. Int. J. Plast. 21 (11), 2212–2231.

Carstensen, C., Conti, S., Orlando, A., 2008. Mixed analytical–numerical relaxation in finite single-slip crystal plasticity. Contin. Mech. Thermodyn. 20, 275–301.

Carstensen, C., Hackl, K., Mielke, A., 2002. Non-convex potentials and microstructures in finite-strain plasticity. Proc. R. Soc. A 458 (2018), 299–317.

Cauchy, A.L., 1847. Méthode générale pour la résolution des systèmes d'équations simultanées. Compte Rendu à l'Académie des Sciences.

Choksi, R., Del Piero, G., Fonseca, I., Owen, D.R., 1999. Structural deformations as energy minimizers in models of fracture and hysteresis. Math. Mech. Solids 4, 321–356.

Christensen, K., Moloney, N.R., 2005. Complexity and Criticality, Vol. 1. World Scientific Publishing Company.

Clayton, J.D., 2010. Nonlinear Mechanics of Crystals, Vol. 177. Springer Science & Business Media.

Conti, S., Zanzotto, G.A., 2004. Variational model for reconstructive phase transformations in crystals, and their relation to dislocations and plasticity. Arch. Ration. Mech. Anal. 173, 69–88.

Cundall, P.A., Strack, O.D., 1979. A discrete numerical model for granular assemblies. Geotechnique 29, 47–65.

Dafalias, Y.F., 1998. Plastic spin: necessity or redundancy? Int. J. Plast. 14 (9), 909–931.

Davini, C., 2001. Some remarks on the continuum theory of defects in solids. Int. J. Solids Struct. 38 (6–7), 1169–1182.

Dequiedt, J.L., 2023. Slip system interactions in BCC single crystals: System de-activation and segregation. Mech. Mater. 184, 104730.

Devincre, B., Kubin, L.P., Lemarchand, C., Madec, R., 2001. Mesoscopic simulations of plastic deformation. Mater. Sci. Eng. A 309, 211–219.

Duistermaat, J.J., Kolk, J.A.C., 1999. Lie Groups. Springer Verlag, Berlin.

Efendiev, Y.R., Truskinovsky, L., 2010. Thermalization of a driven bi-stable FPU chain. Contin. Mech. Thermodyn. 22, 679–698.

Elder, K.R., Grant, M., 2004. Modeling elastic and plastic deformations in nonequilibrium processing using phase field crystals. Phys. Rev. E 70 (5), 051605.

Engel, P., 2012. Geometric Crystallography: An Axiomatic Introduction To Crystallography. Springer Science & Business Media.

Epstein, M., Elzanowski, M., 2007. Material Inhomogeneities and their Evolution. Springer, Berlin.

Epstein, M., Maugin, G., 1996. On the geometrical material structure of anelasticity. Acta Mech. 115, 119–131.

Ericksen, J.L., 1970. Nonlinear elasticity of diatomic crystals. Int. J. Solids Struct. 6 (7), 951–957.

Ericksen, J.L., 1973. Loading devices and stability of equilibrium. In: Dickey, R.W. (Ed.), Nonlinear Elasticity. Academic Press, New York, pp. 161–173.

Ericksen, J.L., 1977. Special topics in elastostatics. Adv. Appl. Mech. 17, 189.

Ericksen, J.L., 1980. Some phase transitions in crystals. Arch. Ration. Mech. Anal. 73, 99–124.

Ericksen, J.L., 1989. Weak martensitic transformations in Bravais lattices. Arch. Ration. Mech. Anal. 107, 23–36.

Fathallah, K., Chenaoui, A., Darrieulat, M., Dogui, A., 2019. Material rotating frame, rate-independent plasticity with regularization of Schmid law and study of channel-die compression. Math. Mech. Solids 24 (1), 18–39.

Featherstone, N.H., Neighbours, J.R., 1963. Elastic constants of tantalum, tungsten, and molybdenum. Phys. Rev. 130 (4), 1324–1333.

Ferrero, E.E., Jagla, E.A., 2019. Criticality in elastoplastic models of amorphous solids with stress-dependent yielding rates. Soft Matter 15, 9041.

Fisher, D.S., 1998. Collective transport in random media: from superconductors to earthquakes. Phys. Rep. 301 (1–3), 113–150.

Folkins, I., 1991. Functions of two-dimensional Bravais lattices. J. Math. Phys. 32, 1965.

Fonseca, I., 1987. Variational methods for elastic crystals. Arch. Ration. Mech. Anal. 97, 189.

Forest, S., 1998. Modeling slip, kink and shear banding in classical and generalized single crystal plasticity. Acta Mater. 46 (9), 3265–3281.

Franz, S., Spigler, S., 2017. Mean-field avalanches in jammed spheres. Phys. Rev. E 95, 022139.

Frenkel, J., 1939. On the theory of plastic deformation and twinning. J. Phys. 1, 137–149.

Gauss, C.F., 1809. Theoria Motus Corporum Coelestium in: Sectionibus Conicis Solem Ambientium. Hamburgi Sumtibus Frid. Perthes et I. H. Besser.

Goh, W.L., Zheng, Y., Yuan, J., Ng, K.W., 2017. Effects of hardness of steel on ceramic armour module against long rod impact. Int. J. Impact Eng. 109, 419–426.

Guo, Y., Curtis, J.S., 2015. Discrete element method simulations for complex granular flows. Annu. Rev. Fluid Mech. 47, 21–46.

Gupta, A., Steigmann, D.J., Stölken, J.S., 2007. On the evolution of plasticity and incompatibility. Math. Mech. Solids 12 (6), 583–610.

Gurtin, M.E., 2000. On the plasticity of single crystals: free energy, microforces, plastic-strain gradients. J. Mech. Phys. Solids 48 (5), 989–1036.

Hähner, P., Bay, K., Zaiser, M., 1998. Fractal dislocation patterning during plastic deformation. Phys. Rev. Lett. 81 (12), 2470–2473.

Han, W., Reddy, B.D., 2012. Plasticity: Mathematical Theory and Numerical Analysis, Vol. 9. Springer Science & Business Media.

Hartley, C.S., Kysar, J.W., 2020. Plane strain deformation by slip in FCC crystals. Int. J. Plast. 133, 102842.

Heslot, F., Baumberger, T., Perrin, P., Caroli, B., Caroli, C., 1994. Creepstick–slipanddryfriction dynamics: experiment and a heuristic model. Phys. Rev. E 49 (6), 4973–4988.

Hestenes, M.R., Stiefel, E., 1952. Methods of conjugate gradients for solving linear systems. J. Res. Natl. Bur. Stand. 49 (6), 409–436.

Hill, R., 1979. Aspects of invariance in solid mechanics. Adv. Appl. Mech. 18, 1–75.

Hochrainer, T., Sandfeld, S., Zaiser, M., Gumbsch, P., 2014. Continuum dislocation dynamics: towards a physical theory of crystal plasticity. J. Mech. Phys. Solids 63, 167–178.

Ispánovity, P.D., Laurson, L., Zaiser, M., Groma, I., Zapperi, S., Alava, M.J., 2014. Avalanches in 2D dislocation systems: Plastic yielding is not depinning. PRL 112, 235501.

Jezdan, G., Behr, F., Dolzmann, G., Hackl, K., 2023. A study of energies in pressure dependent plasticity–mathematical model and mechanical analogies. PAMM 22 (1), e202200160.

Johnson, G.R., Cook, W.H., 1983. A constitutive model and data for metals subjected to large strains, high strain rates and high. In: Proceedings of the 7th International Symposium on Ballistics. pp. 541–547.

Junker, P., Hackl, K., 2013. A condensed variational model for thermo-mechanically coupled phase transformations in polycrystalline shape memory alloys. J. Mech. Behav. Mater. 22 (3–4), 111–118.

Kardar, M., 1998. Nonequilibrium dynamics of interfaces and lines. Phys. Rep. 301 (1–3), 85–112.
Kaxiras, E., Boyer, L.L., 1994. Energetics of large lattice strains: Application to silicon. Phys. Rev. B 50, 1535.
Koslowski, M., Cuitino, A.M., Ortiz, M., 2002. A phase-field theory of dislocation dynamics, strain hardening and hysteresis in ductile single crystals. J. Mech. Phys. Solids 50 (12), 2597–2635.
Krebs, J., Rao, S.I., Verheyden, S., Miko, C., Goodall, R., Curtin, W.A., Mortensen, A., 2017. Cast aluminium single crystals cross the threshold from bulk to size-dependent stochastic plasticity. Nat. Mater. 16 (7), 730–736.
Le Doussal, P., Müller, M., Wiese, K.J., 2012. Equilibrium avalanches in spin glasses. Phys. Rev. B 85.
Lehtinen, A., Costantini, G., Alava, M.J., Zapperi, S., Laurson, L., 2016. Glassy features of crystal plasticity. Phys. Rev. B 94, 064101.
Levitas, V.I., 1998. A new look at the problem of plastic spin based on stability analysis. J. Mech. Phys. Solids 46 (3), 557–590.
Li, L., Anderson, P.M., Lee, M.G., Bitzek, E., Derlet, P., Van Swygenhoven, H., 2009. The stress-strain response of nanocrystalline metals: a quantized crystal plasticity approach. Acta Mater. 57, 812–822.
Li, L., Lee, M.-G., Anderson, P.M., 2012. Probing the relation between dislocation substructure and indentation characteristics using quantized crystal plasticity. J. Appl. Mech. 79, 031009.
Lubliner, J., 2008. Plasticity Theory. Courier Corporation.
McDowell, David.L., 2018. Multiscale crystalline plasticity for materials design. In: Computational Materials System Design. pp. 105–146.
McHugh, P.E., 2004. Introduction to crystal plasticity theory. In: Mechanics of Microstructured Materials. Springer Vienna, Vienna, pp. 125–171.
Michel, L., 2001. Fundamental concepts for the study of crystal symmetry. Phys. Rep. 341, 265–336.
Mielke, A., 2003. Energetic formulation of multiplicative elasto-plasticity using dissipation distances. Contin. Mech. Thermodyn. 15 (4), 351–382.
Mielke, A., Truskinovsky, L., 2012. From discrete visco-elasticity to continuum rate-independent plasticity: rigorous results. Arch. Ration. Mech. Anal. 203 (2), 577–619.
Miller, R.E., Tadmor, E., 2002. The quasicontinuum method: Overview, applications and current directions. J. Comput.-Aided Mater. Des. 9, 203–239.
Müller, M., Wyart, M., 2015. Marginal stability in structural, spin, and electron glasses. Annu. Rev. Condens. Matter Phys. 6, 177.
Nabarro, F.R.N., 1947. Dislocations in a simple cubic lattice. Proc. Phys. Soc. 59 (2), 256.
Noll, W., 1967. Materially uniform simple bodies with inhomogeneities. Arch. Ration. Mech. Anal. 27, 1–32.
Ovaska, M., Laurson, L., Alava, M.J., 2015. Quenched pinning and collective dislocation dynamics. Sci. Rep. 5, 10580.
Parry, G., 1976. On the elasticity of monatomic crystals. Math. Proc. Cambridge Philos. Soc. 80, 189–211.
Parry, G., 1977. On the crystallographic point groups and on Cauchy symmetry. Math. Proc. Cambridge Philos. Soc. 82, 165–175.
Parry, G.P., 1998. Low-dimensional lattice groups for the continuum mechanics of phase transitions in crystals. Arch. Ration. Mech. Anal. 145, 1.
Pázmándi, F., Zaránd, G., Zimányi, G.T., 1999. Self-organized criticality in the hysteresis of the Sherrington-Kirkpatrick model. Phys. Rev. Lett. 83, 1034.
Peierls, R., 1940. The size of a dislocation. Proc. Phys. Soc. 52 (1), 34.
Perchikov, N., Aboudi, J., 2020. Micromechanical analysis of hyperelastic composites with localized damage using a new low-memory Broyden-step-based algorithm. Arch. Appl. Mech. 90, 47–85.
Petryk, H., 2005. Thermodynamic conditions for stability in materials with rate-independent dissipation. Phil. Trans. R. Soc. A 363 (1836), 2479–2515.
Pitteri, M., 1984a. Reconciliation of local and global symmetries of crystals. J. Elasticity 14, 175.
Pitteri, M., 1984b. Reconciliation of local and global symmetries of crystals. J. Elasticity 14, 175–190.
Pitteri, M., Zanzotto, G., 2002. Continuum Models for Phase Transitions and Twinning in Crystals. CRC Press.
Popov, V.L., Gray, J.A.T., 2012. Prandtl-Tomlinson model: History and applications in friction, plasticity, and nanotechnologies. ZAMM Z. Angew. Math. Mech. 92 (9), 683–708.
Prandtl, L., 1928. Ein Gedankenmodell zur kinetischen Theorie der festen Korper. Z. Angew. Math. Mech. 8, 85–106.
Puglisi, G., Truskinovsky, L., 2005. Thermodynamics of rate-independent plasticity. J. Mech. Phys. Solids 53 (3), 655–679.
Reina, C., Conti, S., 2014. Kinematic description of crystal plasticity in the finite kinematic framework: A micromechanical understanding of f= fefp. J. Mech. Phys. Solids 67, 40–61.
Rice, J.R., 1971. Inelastic constitutive relations for solids: an internal-variable theory and its application to metal plasticity. J. Mech. Phys. Solids 19 (6), 433–455.
Rorato, R., Arroyo, M., Gens, A., Andò, E., Viggiani, G., 2021. Image-based calibration of rolling resistance in discrete element models of sand. Comput. Geotech. 131, 103929.
Roters, F., Eisenlohr, P., Hantcherli, L., Tjahjanto, D.D., Bieler, T.R., Raabe, D., 2010. Overview of constitutive laws, kinematics, homogenization and multiscale methods in crystal plasticity finite-element modeling: Theory, experiments, applications. Acta Mater. 58 (4), 1152–1211.
Ruscher, C., Rottler, J., 2019. Residual stress distributions in athermally deformed amorphous solids from atomistic simulations. arXiv:1908.01081.
Salman, O.U., Baggio, R., Bacroix, B., Zanzotto, G., Gorbushin, N., Truskinovsky, L., 2021. Discontinuous yielding of pristine micro-crystals. C. R. Phys. 22 (S3), 201–248.
Salman, O.U., Truskinovsky, L., 2011. Minimal integer automaton behind crystal plasticity. Phys. Rev. Lett. 106 (17), 175503.
Salman, O.U., Truskinovsky, L., 2012. On the critical nature of plastic flow: One and two dimensional models. Internat. J. Engrg. Sci. 59, 219–254.
Salmenjoki, H., Laurson, L., Alava, M.J., 2021. Avalanche correlations and stress–strain curves in discrete dislocation plasticity. Phys. Rev. Mater. 5, 073601.
Schröder, Jörg., Hackl, Klaus., 2013. Plasticity and Beyond: Microstructures, Crystal-Plasticity and Phase Transitions, Vol. 550. Springer Science & Business Media.
Shang, B., Guan, B., Barrat, J.-L., 2020. Elastic avalanches reveal marginal behavior in amorphous solids. Proc. Natl. Acad. Sci. USA 117, 86.
Simo, Juan.C., Thomas, JR.Hughes., 2010. Computational Inelasticity, Vol. 7. Springer Science & Business Media.
Sornette, D., 2006. Critical Phenomena in Natural Sciences: Chaos, Fractals, Selforganization and Disorder: Concepts and Tools. Springer Science & Business Media.
Steigmann, D.J., 2023. A Course on Plasticity Theory, Vol. 7. Oxford University Press.
Svendsen, B., Bargmann, S., 2010. On the continuum thermodynamic rate variational formulation of models for extended crystal plasticity at large deformation. J. Mech. Phys. Solids 58 (9), 1253–1271.
Truskinovsky, L., Vainchtein, A., 2004. The origin of nucleation peak in transformational plasticity. J. Mech. Phys. Solids 52 (6), 1421–1446.
Tyukodi, B., Vandembroucq, D., Maloney, C.E., 2019. Avalanches, thresholds, and diffusion in mesoscale amorphous plasticity. Phys. Rev. E 100, 043003.
Waal, B.W., 1990. A general procedure to derive magic strain tensors. Acta Crystallogr. Sect. A 46, 17.
Walpole, L.J., 1986. The elastic shear moduli of a cubic crystal. J. Phys. D: Appl. Phys. 19, 457–462.
Wang, J., Yip, S., Phillpot, S.R., Wolf, D., 1993. Crystal instabilities at finite strain. Phys. Rev. Lett. 71, 4182.
Wang, T., Zhang, F., Furtney, J., Damjanac, B., 2022. A review of methods, applications and limitations for incorporating fluid flow in the discrete element method. J. Rock Mech. Geotech. Eng. 14 (3), 1005–1024.
Weiss, J., Rhouma, W.B., Richeton, T., Dechanel, S., Louchet, F., Truskinovsky, L., 2015. From mild to wild fluctuations in crystal plasticity. Phys. Rev. Lett. 114 (10), 105504.
Weiss, J., Zhang, P., Salman, O.U., Liu, G., Truskinovsky, L., 2021. Fluctuations in crystalline plasticity. C. R. Phys. 22 (S3), 1–37.
Zener, C., 1948. Elasticity and Anelasticity of Metals. University of Chicago, Chicago.
Zepeda-Ruiz, L., Stukowski, A., Oppelstrup, T., et al., 2017. Probing the limits of metal plasticity with molecular dynamics simulations. Nature 550, 492–495.
Zhang, P., Salman, O.U., Weiss, J., Truskinovsky, L., 2020a. Variety of scaling behaviors in nanocrystalline plasticity. Phys. Rev. E 102 (2), 023006.
Zhang, P., Salman, O.U., Weiss, J., Truskinovsky, L., 2020b. Variety of scaling behaviors in nanocrystalline plasticity. Phys. Rev. E 102, 023006.
Zhang, X., Zhang, X.-C., Li, Q., Shang, F.-L., 2016. Strain avalanches in microsized single crystals: Avalanche size predicted by a continuum crystal plasticity model. Chin. Phys. Lett. 33, 106401.